Atmos. Chem. Phys. Discuss., 13, 22151–22220, 2013
www.atmos-chem-phys-discuss.net/13/22151/2013/
doi:10.5194/acpd-13-22151-2013

Atmospheric Chemistry and Physics Discussions

Air-snowpack exchange of bromine, ozone and mercury in the springtime Arctic simulated by the 1-D model PHANTAS – Part 2: Mercury and its speciation

K. Toyota[1,2], **A. P. Dastoor**[3], **and A. Ryzhkov**[3]

[1]Department of Earth and Space Science and Engineering, York University, Toronto, Ontario, Canada
[2]Air Quality Modelling and Integration Section, Environment Canada, Toronto, Ontario, Canada
[3]Air Quality Modelling and Integration Section, Environment Canada, Dorval, Quebec, Canada

Received: 13 July 2013 – Accepted: 19 August 2013 – Published: 26 August 2013

Correspondence to: K. Toyota (kenjiro.toyota@ec.gc.ca)

Published by Copernicus Publications on behalf of the European Geosciences Union.

Abstract

Atmospheric mercury depletion events (AMDEs) refer to a recurring depletion of mercury in the springtime Arctic (and Antarctic) boundary layer, occurring, in general, concurrently with ozone depletion events (ODEs). To close some of the knowledge gaps in the physical and chemical mechanisms of AMDEs and ODEs, we have developed a one-dimensional model that simulates multiphase chemistry and transport of trace constituents throughout porous snowpack and in the overlying atmospheric boundary layer (ABL). Building on the model reported in a companion paper (Part 1: In-snow bromine activation and its impact on ozone), we have expanded the chemical mechanism to include the reactions of mercury in the gas- and aqueous-phases with temperature dependence of rate and equilibrium constants accounted for wherever possible. Thus the model allows us to study the chemical and physical processes taking place during ODEs and AMDEs within a single framework where two-way interactions between the snowpack and the atmosphere are simulated in a detailed, process-oriented manner.

Model runs are conducted for meteorological and chemical conditions representing the springtime Arctic ABL loaded with "haze" sulfate aerosols and the underlying saline snowpack laid on sea ice. Using recent updates for the $Hg + Br \rightleftarrows HgBr$ reaction kinetics, we show that the rate and magnitude of photochemical loss of gaseous elemental mercury (GEM) during AMDEs exhibit a strong dependence on the choice of reaction(s) of HgBr subsequent to its formation. At 253 K, the temperature that is presumably low enough for bromine radical chemistry to cause prominent AMDEs as indicated from field observations, the parallel occurrence of AMDEs and ODEs is simulated if the reaction HgBr + BrO is assumed to produce a thermally stable intermediate, Hg(OBr)Br, at the same rate constant as the reaction HgBr + Br. On the contrary, the simulated depletion of atmospheric mercury is notably diminished by not allowing the former reaction to occur in the model. Similarly to ozone (reported in the companion paper), GEM is destroyed via bromine radical chemistry more vigorously in the snowpack interstitial air than in the ambient air. However, the impact of such in-snow sink of

ACPD
13, 22151–22220, 2013

GEM is found to be often masked by the re-emissions of GEM from the snow following the photo-reduction of Hg(II) deposited from the atmosphere. Gaseous oxidized mercury (GOM) formed in the ambient air is found to undergo fast "dry deposition" to the snowpack by being trapped on the snow grains in the top ~ 1 mm layer. We hypothesize that liquid-like layers on the surface of snow grains are connected to create a network throughout the snowpack, thereby facilitating the vertical diffusion of trace constituents trapped on the snow grains at much greater rates than one would expect inside solid ice crystals. Nonetheless, on the timescale of a week simulated in this study, the signal of atmospheric deposition does not extend notably below the top few centimeters of the snowpack. We propose and show that particulate-bound mercury (PBM) is produced mainly as $HgBr_4^{2-}$ by taking up GOM into bromide-enriched aerosols after ozone is significantly depleted in the air mass. In the Arctic, "haze" aerosols may thus retain PBM in ozone-depleted air masses, allowing the airborne transport of oxidized mercury from the area of its production farther than in the form of GOM. Temperature dependence of thermodynamic constants calculated in this study for Henry's law and aqueous-phase halide complex formation of Hg(II) species is a critical factor for this proposition, calling for experimental verification. The proposed mechanism may explain a major part of changes in the GOM-PBM partitioning with seasons, air temperature and the concurrent progress of ozone depletion as observed in the high Arctic. The net deposition of mercury to the surface snow is shown to increase with the thickness of the turbulent ABL and to correspond well with the column amount of BrO in the atmosphere.

1 Introduction

A dynamic exchange of halogens between the ocean, sea ice, snowpack, and the atmosphere is a main driver for the frequent occurrence of ozone depletion events (ODEs) and atmospheric mercury depletion events (AMDEs) in the springtime polar boundary layer (Simpson et al., 2007; Steffen et al., 2008). Virtually concurrent occurrence of ODEs and AMDEs indicates a major contribution from common reactants,

ACPD
13, 22151–22220, 2013

most likely gaseous bromine radicals (Br and BrO) associated with a so-called "bromine explosion" (Platt and Lehrer, 1996; Wennberg, 1999; Schroeder et al., 1998). During the AMDEs, gaseous elemental mercury (GEM) is photochemically transformed to oxidized mercury compounds in the gaseous and/or particulate form. They are then removed from the atmosphere via dry and wet deposition much more efficiently than GEM, entering snowpack that covers most of the land/water surfaces until summer melt (Lu et al., 2001; Lindberg et al., 2002). Subsequently, the oxidized mercury can be methylated via biotic and abiotic processes. Bio-accumulation of mono-methyl mercury through aquatic food chains increases a risk of adverse toxicological impacts on wild life and ultimately imposes health concerns on northern indigenous people consuming fish and marine mammals as major diets (AMAP, 2011). However, the actual impacts of AMDEs on high mercury levels detected from northern wild life and humans remain uncertain for the following reasons.

First, field measurements of mercury in the snowpack and overlying ambient air, including but not limited to those in the polar region, quite often indicate the photo-reduction of deposited oxidized mercury back to GEM on timescales of days to weeks (Lalonde et al., 2002, 2003; Steffen et al., 2002; Ariya et al., 2004; Kirk et al., 2006; Johnson et al., 2008). This raises a question as to how much of the mercury deposited during the AMDEs may sustain until snowmelt when mercury contaminating the snow is supposed to enter aquatic food chains. Vertical fluxes of GEM and gaseous oxidized mercury (GOM) determined from in-situ measurements at Barrow, Alaska, depicted the net mercury deposition to the snow as a relatively small residual between the net GOM deposition and the net GEM emission during and after AMDEs (Brooks et al., 2006). By simply assigning a retention timescale of about two weeks in the snowpack against the photo-reduction induced re-emission of deposited mercury, some atmospheric mercury chemical-transport models satisfactorily simulated decrease in the ground-level mixing ratios of GEM during the AMDEs and subsequent increase above the hemispheric background as observed at Arctic coastal sites (Dastoor et al., 2008; Holmes et al., 2010). These models estimated that about 40 % of deposited mercury is

ACPD
13, 22151–22220, 2013

preserved in the Arctic snowpack until entering the surface waters via snowmelt (Ariya et al., 2004; Dastoor et al., 2008; Holmes et al., 2010). However, as pointed out by a mass balance inventory (Outridge et al., 2008) and more recently by model studies elaborating the air-sea exchange of mercury (Fisher et al., 2012; Durnford et al., 2012), this budget picture could have overstated the role of atmospheric deposition during the AMDEs by neglecting a large reservoir of mercury in surface seawater sourced via rivers surrounding the Arctic Ocean. On the other hand, generally higher GEM concentrations over the ice-covered Arctic Ocean than over the nearby ice-free ocean were indicated from yet-scarce field observations in summer (Aspmo et al., 2006; Hirdman et al., 2009; Sommar et al., 2010), implying some significant connection with atmospheric deposition during the AMDEs. It appears that the pieces of evidence obtained so far are insufficient to draw a coherent conclusion to the problem.

Second, owing to many unknowns and substantial uncertainties in the kinetics and mechanisms of mercury oxidation and in the subsequent behavior of oxidized mercury against scavenging processes in the atmosphere, it is quite difficult presently to develop process-based models for simulating how fast mercury is oxidized and is then deposited to the snow/ice covered surfaces during the AMDEs. As reviewed in Subir et al. (2011), gas-phase kinetics data for Hg(0) oxidation from laboratory experiments are subject to potentially large artifacts associated with rate determination techniques and unwanted secondary reactions, leaving error bars often by more than an order of magnitude in the derived rate constants. Additionally, the oxidation of Hg(0) to Hg(II) is likely to proceed via multiple reaction steps, whereas gauging the kinetics for all of the probable reaction steps operating in the natural environment is a formidable task. For example, the reaction Hg + Br initially produces HgBr (Donohoue et al., 2006):

$$\mathrm{Hg} + \mathrm{Br} \rightarrow \mathrm{HgBr} \qquad \text{(R1)}$$

ACPD
13, 22151–22220, 2013

which either dissociates back to the original reactions or undergoes further reactions with Br-atoms in a simple Hg-Br system such as reaction vessels (Goodsite et al., 2004, 2012; Balabanov et al., 2005):

$$HgBr \rightarrow Hg + Br \quad \text{(R2)}$$

$$HgBr + Br \rightarrow HgBr_2 \quad \text{(R3)}$$

$$HgBr + Br \rightarrow Hg + Br_2. \quad \text{(R4)}$$

Goodsite et al. (2004) theoretically estimated rate constants for Reactions (R1)–(R3) and their temperature dependence, whilst the same authors revised their own estimates later in Goodsite et al. (2012). They speculated that estimated increase in the rate constant of Reaction (R2) with temperature would be one of the key factors for the termination of AMDEs towards the summer and that OH-radicals and I-atoms may also react with HgBr as in Reaction (R3) to give thermally stable products, Hg(OH)Br and HgBrI, respectively. Calvert and Lindberg (2004) conjectured yet other reaction steps, where HgBr first reacts with BrO to give Hg(OBr)Br, which then photolyzes to Hg(O)Br + Br, and eventually produces Hg(OH)Br:

$$HgBr + BrO \rightarrow Hg(OBr)Br \quad \text{(R5)}$$

$$Hg(OBr)Br + h\nu \rightarrow Hg(O)Br + Br \quad \text{(R6)}$$

$$Hg(O)Br + HO_2 \rightarrow Hg(OH)Br + O_2. \quad \text{(R7)}$$

Rate constants for these reactions were adjusted heuristically in their box model to simulate a conceivably reasonable timescale of AMDEs against that of ODEs (Calvert and Lindberg, 2004). In laboratory experimental systems, some of the reactions are mediated at least partially on the chamber wall surface (Ariya et al., 2002; Raofie and Ariya, 2004). But it remains unknown whether or not surface-mediated pathways can enhance the overall oxidation rates of Hg(0) by Br and/or BrO on various environmental surfaces as well.

ACPD
13, 22151–22220, 2013

Here we note that, unlike a few mechanistic box and one-dimensional (1-D) models published to date (e.g., Saiz-Lopez et al., 2008; Xie et al., 2008), three-dimensional (3-D) chemical-transport models of mercury have generally assigned the temporal and spatial distributions of Hg(0) oxidants in the polar boundary layer in a simpler fashion than simulating a full suite of gaseous and heterogeneous reactions involved (e.g., Dastoor et al., 2008; Holmes et al., 2010). Therefore, to some extent, the mechanism of mercury redox reactions and their rate constants are empirically defined to simulate AMDEs realistically in such 3-D models. This practice may be justified for the moment because we have not yet established a solid understanding of the chemical and physical mechanisms for reactive halogen release into the polar boundary layer (Abbatt et al., 2012) and of the re-emission of deposited mercury as noted earlier. But we certainly need to employ a more sophisticated approach in the 3-D models if we are to better assess how AMDEs and resultant mercury deposition might respond to varying environmental factors including climate change. A recent work by Parrella et al. (2012) made a step forward along this line, as their 3-D model of mercury also simulated the gaseous and heterogeneous chemistry of bromine in the global troposphere, even though the model relied on ad-hoc parameters in constraining the source term of reactive bromine from sea-salt aerosols and took no account of the sources from polar snow/ice packs.

Once oxidized, mercury retains greater Henry's law and surface adsorption coefficients and is thus more prone to uptake onto aerosols, clouds and various surfaces than in the form of GEM (Subir et al., 2012). In the polar boundary layer, oxidized mercury exists as either GOM or particulate-bound mercury (PBM) (Brooks et al., 2006, 2008; Cobbett et al., 2007; Steen et al., 2011), whilst dry and wet deposition rates can be vastly different between GOM and PBM (Brooks et al., 2006; Skov et al., 2006; Amos et al., 2012). This aspect has been poorly handled in chemical-transport models of mercury in general (Amos et al., 2012). As anticipated from thermodynamic grounds, temperature and the amount of host aerosols do appear to influence the partitioning between GOM and PBM in the polar boundary layer, but other factors (such as aerosol

ACPD
13, 22151–22220, 2013

composition) remain to be characterized to derive a more compact relationship for the GOM-PBM partitioning (Cobbett et al., 2007; Brooks et al., 2008).

This study builds on a companion paper on the simulation of reactive bromine release and ODEs in the springtime Arctic by using a 1-D air-snowpack model, PHANTAS (a model of PHotochemistry ANd Transport in Air and Snowpack) (Toyota et al., 2013). Here we investigate potential key steps leading to the net oxidation of GEM in the atmospheric boundary layer (ABL) and the snowpack interstitial air (SIA) during AMDEs, and the fate of oxidized mercury in the ABL, in the SIA and on the surface of snow grains within the snowpack. The multiphase chemical mechanism of PHANTAS is expanded to include mercury chemistry in the gas- and condensed-phases, with temperature-dependent reaction rate and equilibrium constants employed wherever possible. Previous mechanistic box and 1-D models of the same kind neglected either an explicit treatment of condensed-phase chemistry (Saiz-Lopez et al., 2008) or temperature dependence in the gas- and aqueous-phase reactions of mercury (Xie et al., 2008). On the basis of our mercury chemical mechanism, a potential link is indicated for the first time between the GOM-PBM partitioning during AMDEs and the partitioning of inorganic bromine changing concurrently with the depletion of ozone.

2 Model description

2.1 General framework

PHANTAS is a 1-D model that represents the multiphase chemistry and transport of trace constituents from the bottom of saline snowpack and to beyond the turbulent ABL. The model is primarily used to investigate the role of halogen chemistry on the processes responsible for ODEs and AMDEs in polar regions. Toyota et al. (2013) describes the transport and chemical processes, other than those related to mercury, included in the model. Here we provide a general overview of the model, followed by a description of the mercury chemistry component in the next section.

ACPD
13, 22151–22220, 2013

The chemical mechanism of PHANTAS has been adapted from that originally developed for a box model of multiphase halogen chemistry involving deliquesced sea-salt aerosols in the marine boundary layer, called SEAMAC (Size-sEgregated Aerosol model for Marine Air Chemistry) (Toyota et al., 2004). A common set of reactions are employed to describe a gas-aerosol system in the atmosphere and a gas-brine system in the snowpack. We assume that the surface of snow grains is covered with a liquid-like layer (LLL), into which all the in-snow solutes are excluded from solid ice. To what extent this assumption makes sense is a matter of debate (e.g., Mulvaney et al., 1988; Rosenthal et al., 2007; Barret et al., 2011; Thomas et al., 2011; Asaduzzaman et al., 2012) but is beyond the scope of this study. Here we employ a simple thermodynamic parameterization by Cho et al. (2002) to predict the volume fraction of the LLL in the snow grains from the bulk concentrations of major ionic components (Cl^-, NO_3^-, etc.) contained in the snow. Atmospheric aerosols in the present version of PHANTAS are composed only of "sulfate aerosols", viz. the mixture of NH_4HSO_4-H_2SO_4-H_2O as a major aerosol substrate and a predominant component of Arctic haze. Thus, the model does not account for halogen release from airborne sea-salt particles associated with blowing snow events (e.g., Yang et al., 2008). Also, PHANTAS does not retain a capability carried by SEAMAC of simulating size-resolved aerosol chemistry (Toyota et al., 2001).

In the present model configuration, the vertical grid consists of 55 layers, among which 22 layers represent the porous snowpack of 35 cm in depth as typically observed on sea ice in the springtime Arctic (Warren et al., 1999) and 33 layers represent the ABL as well as some extra layers in the free troposphere. Spacing between the grid cells is not uniform and is made very small around the atmosphere-snowpack interface (e.g., $\Delta z = 10^{-4}$ m at the top of the snowpack and $\Delta z = 10^{-2}$ m at the bottom of the atmosphere) to resolve sharp changes in tracer diffusivity and in reaction pathways across this region. The grid spacing in the entire snowpack (22 layers) and in the atmosphere below 10 m above the snow surface (12 layers) remains the same between model runs, while it changes between the model runs above the 10 m level in the

ACPD
13, 22151–22220, 2013

atmosphere (21 layers) according to the diagnosed height of the turbulent ABL (Z_{ABL}) at noon when Z_{ABL} is at maximum.

The profile of vertical diffusivity for tracers in the atmospheric boundary layer and its diurnal variations are diagnosed by solving a set of micro-meteorological equations from several pre-defined input parameters including wind speed at a reference height (2 m in this study), diurnally-varying sensible heat fluxes at the air-snowpack interface (typical of March in Beaufort Sea, Persson et al., 2002), static stability (or the Brunt-Väisälä frequency, $N = 0.031\ s^{-1}$) in the free troposphere (Steeneveld et al., 2007), and the Coriolis parameter (at 71° N). Tracer diffusivity above Z_{ABL} is assumed to be controlled by molecular diffusion for gases and by Brownian diffusion for aerosols. Molecular diffusivity (D_g) for GEM is calculated based on an empirical formula by Massman (1999) and is re-used for other gaseous mercury species (XHg) with molar-mass based scaling, i.e. $D_{g,XHg} = D_{g,GEM} \times \sqrt{M_{GEM}/M_{XHg}}$. For non-mercury species, D_g is calculated by using an empirical formula and associated parameters from Fuller et al. (1966, 1969). In the SIA, molecular diffusion is assumed to control the vertical transfer of gaseous tracers while being scaled down by 50 % to account for the effect of tortuosity (Albert and Shultz, 2002). The effect of wind pumping in the SIA is represented in the form of effective diffusivity, which is superimposed on molecular diffusivity when the surface air flow is diagnosed to be aerodynamically rough and is thus likely to develop persistent pressure perturbations along the mean streamline of wind over the snow micro-topography (e.g., Cunningham and Waddington, 1993).

Lack of consensus on actual mechanisms that facilitate the mass transport in experimentally-prepared ice samples (Huthwelker et al., 2006) and in natural snowpacks (Domine et al., 2004, 2008) renders the vertical transfer rates of trace constituents trapped in/on ice subject to great uncertainties. As noted above, there is also an issue of the uncertainty in the partitioning of dissolved constituents between the surface disordered region (viz. the LLL) and the interior of solid ice. Here it is assumed first that the LLL is connected to create a network throughout the snowpack (e.g., Colbeck, 1979; Wolff and Paren, 1984; Rosenthal et al., 2007). Then the vertical transfer rates of

ACPD
13, 22151–22220, 2013

dissolved constituents are approximated by the temperature-dependent self-diffusion coefficient (D_{aq}) of supercooled water (e.g., Nasello et al., 2007; Gladich et al., 2011), adopted here from the Smith and Kay (1999) parameterization while being scaled down by 50 % to account for the tortuosity of the hypothetical LLL network (Toyota et al., 2013, Sect. 2.8). A sensitivity of model results to this network assumption is explored by turning D_{aq} to zero in one of the model runs.

The transfer rates of gaseous tracers across the interface between the atmosphere and the SIA are controlled largely by vertical diffusivity on the atmosphere side, because very small Δz is adopted on the snowpack side. For species like Br_2 sourced mainly in the snowpack, net transfer occurs generally from the SIA to the atmosphere. On the contrary, species like HBr undergo net transfer from the atmosphere to the SIA most of the time. To calculate the vertical fluxes of species contained in aerosols at the bottom of the atmosphere, we assign the dry deposition velocity of sub-μm sulfate aerosols at $\sim 0.02\,\mathrm{cm\,s^{-1}}$ based on the Petroff and Zhang (2010) parameterization. This results in a one-way transfer of aerosols from the atmosphere to the snowpack, unlike the transfer of gaseous tracers assumed to occur in both ways between the atmosphere and the SIA. We then allocate all the deposited amount of aerosol constituents to the top layer of the snowpack. In reality, aerosols entering the SIA might travel farther than assumed here, but existing theoretical treatments seem to overpredict this in-snow travel distance of aerosols (Harder et al., 1996). According to Petroff and Zhang (2010), the trapping of aerosol particles by snow grains appears to be controlled by poorly characterized phoretic effects.

Actinic fluxes in the atmosphere are calculated with a two-stream algorithm by Kylling et al. (1995), for a clear sky on 30 March at 71° N with a total column ozone of 400 Dobson units over the snow surface with a wavelength-independent snow albedo of 0.9 (Warren and Wiscombe, 1980). The actinic flux also penetrates the snowpack while being attenuated with depth in most cases; in this work, the e-folding depth for the attenuation is assumed to be 7.5 cm (King and Simpson, 2001; Peterson et al., 2002; Qiu et al., 2002; Simpson et al., 2002). We thus neglect the possibility of enhanced actinic

ACPD
13, 22151–22220, 2013

fluxes that can occur near the top of the snowpack under certain conditions (Abbatt et al., 2012).

2.2 Mercury chemical mechanism

Our mercury chemical mechanism has been developed by combining and adapting the mechanisms from other recent models of photochemical interactions between mercury and bromine in the polar boundary layer and in the global troposphere (Calvert and Lindberg, 2004; Hedgecock et al., 2005; Xie et al., 2008; Holmes et al., 2010). Figure 1 illustrates the overview of the mercury mechanism developed here, while Table 1 lists all the mercury reactions and their rate or equilibrium coefficients used. Here we assume that the gas-phase oxidation of GEM is initiated only via reaction with Br-atom to give HgBr (Reaction R1), followed either by its thermal decomposition to Hg + Br (Reaction R2) or by further reactions to give relatively stable Hg(II) products such as Hg(OBr)Br and $HgBr_2$ (e.g., Reactions R3 and R5). It deserves to be mentioned that the rate constant and its temperature dependence for Reaction (R1) theoretically estimated by Goodsite et al. (2012) in their recent work are in excellent agreement with an experimental determination by Donohoue et al. (2006), giving some confidence in this part of the mercury mechanism adopted here.

Previous models often employed reactions between GEM and other oxidants such as BrO, O_3 and OH deemed to occur in the gas phase for the simulation of mercury chemistry in the polar and/or global troposphere (e.g., Dastoor and Larocque, 2004; Selin et al., 2007; Dastoor et al., 2008). As compared to the reaction with atomic Br, however, these latter reactions are believed either not to occur purely in the gas phase or to proceed at much slower rates than determined experimentally (Subir et al., 2011, and references therein). Discrepancies in the reported rate constants imply critical roles played by heterogeneous surface reactions and/or third-body effects in the experimental systems and, by extension, in the natural environment. However, better understanding of mechanistic details is required before we can represent them adequately in the models (Pal and Ariya, 2004; Raofie and Ariya, 2004; Calvert and Lindberg, 2005;

ACPD
13, 22151–22220, 2013

Snider et al., 2008; Subir et al., 2012). Fortunately, all of these uncertainties do not seem to disprove the major role of bromine chemistry as a cause of AMDEs in the polar boundary layer, but the share of Br-atoms against that of BrO-radicals is uncertain owing to error bars associated with the unknown surface and third-body effects (Calvert and Lindberg, 2004; Dastoor et al., 2008; Seigneur and Lohman, 2008; Xie et al., 2008; Subir et al., 2012).

Temperature dependence in the partitioning behavior of Hg(II) between gas- and aqueous-phases has been ignored or under-represented in earlier mercury models (e.g., Xie et al., 2008). Here we address the effects of changing aerosol bromide contents in the gas-aerosol Hg(II) partitioning, in addition to their temperature dependence, in the springtime Arctic context. For this purpose, we calculate the temperature dependence of Henry's law coefficients (K_H) for Hg(II) species and of stability constants (K_{eq}) for Hg(II)-halide coordination complexes that form in the aqueous phase (such as $HgCl_4^{2-}$ and $HgBr_4^{2-}$) by using the van't Hoff equation while taking thermodynamic parameters from the literature if available. For Hg(0), $Hg(OH)_2$ and $HgCl_2$, K_H and its temperature dependence have been determined experimentally (e.g., Sanemasa, 1975; Iverfeldt and Lindqvist, 1980; Lindqvist and Rodhe, 1985; Sommar et al., 2000; Andersson et al., 2008), and therefore the experimental data are favored for use in our model over the thermodynamic estimation. We also postulate the formation of mixed-halide complexes such as $HgCl_3Br^{2-}$ (see Appendix A).

Experimental evidence suggests that the net rate of photo-reduction from Hg(II) to Hg(0) in water and in the LLL on ice is controlled by the abundance and functional characteristics of dissolved organic matter (DOM) mediating the photo-reduction and by impeding effects from co-existent halide anions and dissolved oxygen (e.g., Allard and Arsenie, 1991; Xiao et al., 1995; Si and Ariya, 2008, 2011; Lalonde et al., 2003; Bartels-Rausch et al., 2011). In this study, we do not aim at addressing this problem by breaking down the whole process into a series of reaction elements. Rather, we adopt a simple parameterization in which a prescribed first-order rate constant is employed in the same fashion as Holmes et al. (2010). Here, the rate of gross photo-reduction

ACPD
13, 22151–22220, 2013

from in-snow Hg(II) (regardless of its chemical forms) to Hg(0) is assumed to be either 5 % per day ("slow" photo-reduction scenario, Johnson et al., 2008) or 30 % per day ("fast" photo-reduction scenario, Kirk et al., 2006) on daily mean at the top of the snowpack. However, as the Johnson et al. (2008) study was among the most comprehensive ones conducted in the field under springtime Arctic settings, we use the "slow" photo-reduction scenario as a base case unless otherwise stated. Snow chamber studies from various regions and conditions indicate a major role of UV-B radiation (i.e. $\lambda \lesssim 320$ nm) (Lalonde et al., 2003; Dommergue et al., 2007; Faïn et al., 2007; Johnson et al., 2008; Durnford and Dastoor, 2011). Hence we scale the Hg(II) photo-reduction rate from its daily mean at the top of the snowpack by the calculated photolysis rate of O_3 to $O(^1D)$ changing diurnally and decreasing with depth in the snowpack. Our chemical mechanism also includes the photo-reduction of Hg(II) to Hg(I) by HO_2 and O_2^- in the aqueous phase (Pehkonen and Lin, 1998), but fast re-oxidation of Hg(I) by dissolved O_2 renders this pathway ineffective as a route to the Hg(0) formation (Nazhat and Asmus, 1973; Gårdfeldt and Jonsson, 2003). Aqueous-phase reduction of Hg(II) involving SO_3^{2-} and/or HSO_3^- (e.g., Van Loon et al., 2000, 2001) is neglected in this study. We note, however, that this reduction mechanism might play a role under some circumstances in the Arctic where the anthropogenic emissions of SO_2 are declining and yet abundant in recent decades (Quinn et al., 2007).

2.3 Simulation scenarios

Simulation scenarios are re-used from those adopted in the companion paper for the study of in-snow bromine activation and ozone deletion in the springtime Arctic ABL (Toyota et al., 2013, see Sect. 2.10 and Tables 2–5). In each model run, to calculate vertical diffusivity profiles in the ABL, we assume a constant reference-height (2 m) wind speed ($U_2 = 2\,\mathrm{m\,s^{-1}}$, $4.5\,\mathrm{m\,s^{-1}}$, $8.5\,\mathrm{m\,s^{-1}}$ or $12\,\mathrm{m\,s^{-1}}$) and repeat the same diurnal variations in the surface sensible heat flux ($-5\sim -1\,\mathrm{W\,m^{-2}}$, Persson et al., 2002) over 8 model days. The top height of the turbulent ABL (Z_{ABL}) and the values of turbulent diffusivity throughout the ABL both increase with increasing U_2 and also exhibit

ACPD
13, 22151–22220, 2013

diurnal variations with maxima at noon and minima at midnight (see Fig. 5a–c in Toyota et al., 2013). For example, Z_{ABL} changes over a day between 7 ∼ 44 m, 119 ∼ 128 m, 264 ∼ 268 m and 426 ∼ 429 m at $U_2 = 2\,m\,s^{-1}$, $4.5\,m\,s^{-1}$, $8.5\,m\,s^{-1}$ and $12\,m\,s^{-1}$, respectively (see Fig. 2a in Toyota et al., 2013). The sum of aerodynamic resistance and quasi-laminar layer resistance for $HgBr_2$ to the snow surface at the height of 1 m in the ambient air decreases from the diurnal range of $419 \sim 2070\,s\,m^{-1}$ at $U_2 = 2\,m\,s^{-1}$ to $\sim 58\,s\,m^{-1}$ at $U_2 = 12\,m\,s^{-1}$ (see Fig. 2b in Toyota et al., 2013), dictating changes in apparent dry deposition velocities for $HgBr_2$ and other GOM species as discussed later.

PHANTAS is not fully capable of simulating temperature dependence of potential significance in reactive halogen release from salty snowpack and from other forms of condensate in the atmosphere (Toyota et al., 2013). This is because the model does not handle the precipitation of specific salts from the LLL (and hence changes in brine composition) with decreasing temperatures across the eutectic points of salts being precipitated (e.g., Koop et al., 2000; Sander et al., 2006; Morin et al., 2008), although it does calculate increase in the total brine concentration via freezing out of water in the LLL in an approximate fashion (Cho et al., 2002). This has led to our choice that kinetic rate and thermodynamic equilibrium constants are calculated for temperature at 253 K in the whole model domain for all but sensitivity runs. At this temperature, chloride and bromide contained in the snowpack are expected to be dissolved totally in the LLL rather than precipitated as solid salts (Koop et al., 2000). Although the role of temperature in halogen activation from environmental snow surfaces is an unsettled issue, field observations do suggest the frequent occurrence of ODEs and AMDEs at 253 K (Tarasick and Bottenheim, 2002; Cole and Steffen, 2010; Pöhler et al., 2010). To examine the potential role of temperature in the gas-aerosol partitioning of Hg(II), we have also performed a sensitivity study in which some of the thermodynamic constants for Hg(II) species are re-calculated by assuming temperatures higher than 253 K (see Sect. 3.3).

ACPD
13, 22151–22220, 2013

We have selected the initial concentrations of trace gases and aerosol composition to represent an air mass in the springtime Arctic lower troposphere under a non-ODE/non-AMDE condition (see Table 4 in Toyota et al., 2013). However, for the simplicity of model setup and results interpretation, inorganic bromine is assumed not to exist in the atmosphere in the initial state of each model run. It thus ignores the measurable background of inorganic bromine perhaps present persistently in the free troposphere (e.g., Fitzenberger et al., 2000; Evans et al., 2003). The simulated build-up of reactive bromine in the ABL and in the SIA originates from a photochemical conversion of bromide contained in moderately saline and acidic snowpack, with a negligible source also given by a photolysis of $CHBr_3$. Aerosols are initially composed of the mixture of NH_4HSO_4-H_2SO_4-H_2O only, but they can serve as substrate to retain a significant amount of bromide and Hg(II) species once ozone is depleted in the air (see Sect. 3.1).

Following a box model study on AMDEs by Xie et al. (2008), we start our model runs with the initial mixing ratio of GEM at 0.168 pmol mol^{-1} but here including in the SIA. This mixing ratio is very close to the median ($\sim$ 0.17 pmol mol^{-1}) of GEM mixing ratios observed below 4 km (except in the near-surface air with frequent AMDEs) in the North American Arctic to the north of 50° N during the Arctic Research of the Composition of the Troposphere from Aircraft and Satellites (ARCTAS) campaign in April 2008 (Mao et al., 2010). We note, however, that GEM mixing ratios ($\sim$ 1.7 ng per standard cubic meter or $\sim$ 0.20 pmol mol^{-1}) notably higher than our initial value were measured at altitudes between 1 $\sim$ 7 km over the Beaufort Sea and the Arctic Ocean in April 1998 (Banic et al., 2003). Again, for the sake of simplicity, other forms of mercury (i.e., condensed-phase elemental mercury, gaseous and condensed-phase oxidized mercury) than GEM are assumed not to exist in the entire model domain at the beginning of each run.

ACPD
13, 22151–22220, 2013

3 Results and discussion

3.1 Connections between the chemistry of bromine, ozone and mercury in the ABL

Our model simulates a strong activation of bromine chemistry that occurs inside the porous snowpack under sunlight. It results in very high mixing ratios of inorganic gaseous bromine in the SIA from the first day of each model run, including that of BrO radical exceeding 100 pmol mol^{-1} during the day (Toyota et al., 2013, see Fig. 6), and the evasion of gaseous bromine (mainly as Br_2) from the SIA to the ambient air. For model runs at U_2 = 2.0 m s^{-1}, 4.5 m s^{-1} and 8.5 m s^{-1} discussed here, it takes 2 to 4 days for the abundance of reactive gaseous bromine in the ABL to reach its maximum in each run (Fig. 2a–c, top row). The maxima of atmospheric BrO mixing ratios simulated in these runs (ca. 40 ∼ 50 pmol mol^{-1}) are in the same range as measured previously in the springtime Arctic boundary layer (Tuckermann et al., 1997; Pöhler et al., 2010; Liao et al., 2011). In our model, a principal factor that controls the build-up rate of atmospheric bromine is the thickness of the turbulent ABL; the lower the surface wind speed, the shallower the ABL, and the faster the build-up of bromine in the ABL (Toyota et al., 2013, see Sect. 3.1).

Ozone is then destroyed vigorously in the ambient air (and more so in the SIA) via catalytic reaction cycles involving Br atoms and BrO radicals (Fig. 2a–c, bottom row). Since ozone itself participates in the activation of bromine chemistry via "bromine explosion" (Platt and Lehrer, 1996; Wennberg, 1999), gaseous inorganic bromine stops building up in the air once ozone is depleted below about 5 to 10 nmol mol^{-1} depending on model runs. At this point, a major fate of Br-atoms in the air changes from the reaction with ozone to reactions with aldehydes emitted from the snowpack, first producing HBr and then taken up by sulfate aerosols to maintain high levels of particulate bromide (Fig. 2a–c, top row). The particulate bromide is believed to comprise a major part of "filterable bromine", whose concentrations have been observed to ramp up during ODEs (Barrie et al., 1988; Oltmans et al., 1989; Sander et al., 1997).

ACPD
13, 22151–22220, 2013

Figure 3a–c shows temporal evolution for the mixing ratios of GEM, GOM and PBM in the entire model domain simulated at $U_2 = 2.0\,\mathrm{m\,s^{-1}}$, $4.5\,\mathrm{m\,s^{-1}}$ and $8.5\,\mathrm{m\,s^{-1}}$, respectively. As a result of bromine radical chemistry in the gas-phase, the GEM mixing ratios are simulated to drop in the ABL from the initial mixing ratio of $0.168\,\mathrm{pmol\,mol^{-1}}$ to the temporal minima of about $0.02 \sim 0.05\,\mathrm{pmol\,mol^{-1}}$ depending on model runs. The decrease in atmospheric GEM levels continues until a major shift in the partitioning of inorganic bromine occurs from gaseous species including Br and BrO to particulate bromide in the sulfate aerosols. As discussed above, this shift occurs at the same time as ozone is depleted to low levels, providing one explanation for excellent correlations between ozone and gaseous mercury mixing ratios observed in the course of ODEs/AMDEs from both hemispheres during polar spring (e.g., Schroeder et al., 1998; Ebinghaus et al., 2002).

As long as particulate bromide levels are suppressed via multiphase recycling that drives the "bromine explosion", mercury oxidized from GEM accumulates at first in the gas phase as GOM in the ABL. The composition of GOM simulated in our model is a mixture of several major species (Fig. 4a). A dominant entry pathway from GEM to GOM is a formation of Hg(OBr)Br via Reaction (R1) followed by Reaction (R5) (see Sect. 3.4). Here, the rate constant for the latter reaction (viz. HgBr + BrO) is simply assumed to be the same as that for Reaction (R3) (viz. HgBr + Br), as was done in a box model study by Calvert and Lindberg (2004). According to bond energy calculations, this approximation is quite reasonable (Dibble et al., 2012). However, the rate constant for Reaction (R3) itself has never been measured experimentally but derived only by a theoretical calculation (Goodsite et al., 2004). We will return to this issue in a sensitivity study discussed later. Also hypothetical is the fate of Hg(OBr)Br to give Hg(OH)Br in the gas phase, where we have adopted the same mechanism as Calvert and Lindberg (2004). On the basis of their empirical adjustment of kinetic parameters, the lifetime of Hg(OBr)Br against photolytic decomposition via Reaction (R6) is assumed to be identical to that of HOBr against its photolysis. The product, Hg(O)Br, is then assumed to react with HO_2 via R7 to give Hg(OH)Br, a principal reservoir of GOM

ACPD
13, 22151–22220, 2013

in the present model runs. Subsequently, ion-exchange reactions involving chloride and bromide (despite their trace concentrations most of the time) in sulfate aerosols convert a portion of Hg(OH)Br heterogeneously to $HgBr_2$, HgClBr, $HgCl_2$ and Hg(OH)Cl. The ion-exchange reactions were also incorporated in some of the earlier box models of multiphase mercury chemistry in the marine boundary layer (Hedgecock et al., 2005) and in the polar boundary layer (Xie et al., 2008). However, with no account of reactions to form mixed-ligand Hg(II) (e.g., HgClBr), the ion-exchange reactions appear to have played a minimal role in these models with regard to the GOM speciation. Also, Xie et al. (2008) neglected the photolysis of Hg(OBr)Br and thus predicted this species to be the most abundant in the oxidized mercury pool. The formation of Hg(OBr)Br was not considered in the Hedgecock et al. (2005) model.

Once particulate bromide starts building up in sulfate aerosols after ozone is depleted to sufficiently low levels, GOM is taken up by the aerosols to form PBM (Fig. 3a–c, bottom row). Here, $HgBr_4^{2-}$ makes up a dominant fraction of PBM (Fig. 4a). It arises from the ion-exchange reactions, which, as noted above, affect the speciation of GOM as well. This time, however, high concentrations of bromide thermodynamically favor the formation of a fully coordinated ligand by bromide, i.e. $HgBr_4^{2-}$, to accumulate in the aerosols. To our knowledge, this is the first study in which the role of aerosol composition, especially that of bromide, is indicated as a major factor controlling the GOM-PBM partitioning in the atmosphere. In Sect. 3.3, we will discuss this issue in more detail.

3.2 In-snow oxidation and reduction of mercury

Since daytime mixing ratios of bromine radicals are predicted to be generally higher in the SIA than in the ambient air (Toyota et al., 2013, see Fig. 6), the GEM mixing ratios drop more rapidly in the SIA (but recover to the same levels as in the ambient air in the dark) during the first couple of days in all the model runs. Unlike in the ambient air, the oxidation of GEM does not result in the build-up of GOM in the SIA. Instead, GOM is rapidly taken up by the LLL on the grain surface of the snowpack. As the levels of Hg(II) deposited to the snowpack increase with time, the production of Hg(0) via

ACPD
13, 22151–22220, 2013

photo-reduction of Hg(II) in the LLL starts to dominate the oxidative loss of Hg(0) in the SIA. This is reflected in rapid increase in the GEM mixing ratios in the SIA, reaching daily maxima around the noon near the top of the snowpack. The in-snow recovery of GEM levels migrates downwards from the top layers via gas diffusion in the SIA, as a majority of in-snow Hg(II) originally enters the snowpack via "dry deposition" (or gas diffusion) from the atmosphere and is located within the top few centimeters of the snowpack (see Sect. 3.6). Increasing rates of Hg(II) photo-reduction towards the top of the snowpack also contribute to the stronger in-snow source of GEM in the top layers.

Unique behavior of GEM concentrations in the SIA, sometimes higher and at other times lower than in the overlying ambient air and driven by sunlight, has been observed in the field (e.g., Ferrari et al., 2004, 2005; Fain et al., 2006). Our model results are qualitatively consistent with such observations. However, at the "slow" photo-reduction rates assumed here, i.e., 5 % per day at the top of the snowpack, the recovery of GEM in the ABL remains marginal over the 8-day time span of our model runs. On the other hand, the strong recovery of GEM even in excess of its background concentrations has been observed to occur in the near-surface ambient air at polar coastal sites sometimes as rapid as in less than a day in between AMDEs (Steffen et al., 2002; Brooks et al., 2008; Johnson et al., 2008). Even if we assume the faster photo-reduction rates for in-snow Hg(II), i.e. 30 % per day at the top of the snowpack, on the basis of a field study at the coast of Hudson Bay Kirk et al. (2006), our model does not predict such an intense and rapid GEM recovery in the ambient air (not shown).

Here we note a fundamental limitation of the 1-D model approach in representing spatial inhomogeneity, rather than assuming a deficiency in the chemical and physical schemes of our snowpack model. For example, Hirdman et al. (2009) found changes in air mass to play a major role in the variability of atmospheric GEM concentrations from spring to summer at the Zeppelin mountain station on the western coast of Spitsbergen, whilst Steffen et al. (2013a) indicated that in-snow Hg(II) is reducible to Hg(0) more easily over land than over sea ice near Barrow, Alaska. Additionally, open leads and polynya between the frozen surface of seawater can also be an important source of

ACPD
13, 22151–22220, 2013

GEM to the atmosphere (Aspmo et al., 2006; Outridge et al., 2008; Durnford et al., 2012; Fisher et al., 2012). If we are to reproduce the rate and magnitude of GEM recovery as observed in the polar boundary layer, we would need to account for these processes missing in the present 1-D model; this will be a subject of further study using the framework of a 3-D model to resolve the spatial inhomogeneity of geographic features and changing patterns in air mass transport with time.

3.3 Gas-aerosol partitioning of oxidized mercury: a case in the Arctic boundary layer

Amos et al. (2012) incorporated a parameterization of gas-aerosol Hg(II) partitioning in their global 3-D model of mercury chemistry and transport. The empirical approach by Amos et al. related the GOM-PBM partitioning coefficient to temperature and the total mass of aerosols in such a way that the fraction of PBM will increase with decreasing temperature and increasing aerosol mass. However, their scheme did not account for aerosol composition. They found a reasonable success of the parameterization in reproducing seasonal variations in the gas-aerosol partitioning of Hg(II) observed at North American continental sites, but little was evaluated in the polar boundary layer. On the other hand, multi-year measurements of speciated mercury, viz. GEM, reactive gaseous mercury (RGM) and PBM, at Alert, Canada, identified robust seasonal variations in the RGM-PBM partitioning at this site (Cobbett et al., 2007; Steffen et al., 2013b). The speciation of RGM is defined operationally by a sampling protocol of the instrument with its collection efficiency occasionally subject to notable artifacts (Lyman et al., 2010), but we may consider RGM to be almost equivalent to GOM. Steffen et al. (2013b) showed seasonal transitions in the RGM-to-PBM ratios at Alert to be strongly related to temperature and the mass concentrations of haze aerosols. Our model results here suggest that bromide content in the haze aerosols, rather than the concentration of the haze aerosols themselves, is actually a key player for the determination of ratios between RGM (or GOM) and PBM during the AMDEs (Fig. 4a).

ACPD
13, 22151–22220, 2013

A shift in the GOM-PBM partitioning has a significant consequence for the rate of deposition of oxidized mercury from the atmosphere. As shown in Fig. 4b, the net vertical flux of oxidized mercury from the atmosphere to the snowpack decreases by more than a magnitude after PBM takes over GOM in the partitioning of oxidized mercury. Dry deposition velocities for PBM contained in the sub-μm sulfate aerosols are calculated to be $\sim 0.02\,\mathrm{cm\,s^{-1}}$ in our model runs (Sect. 2.1), whereas apparent dry deposition velocities (defined by a ratio of the vertical flux of a trace constituent against its concentration at the same height) for a majority of GOM species (e.g., $HgBr_2$, Hg(OH)Br, $HgCl_2$) are close to the inverse of aerodynamic resistance and are thus greater than the dry deposition velocities for PBM by an order of magnitude or more (Fig. 5a–i). In other words, GOM will likely undergo localized and intense dry deposition soon after its formation in the atmosphere, whereas the impact of PBM dry deposition will be quite modest locally while extending over greater spatial scales. From the field measurements of vertical fluxes of RGM over the Arctic snow cover, Skov et al. (2006) concluded that the dry deposition velocities of RGM were limited in general by aerodynamic resistance to the snow surface, in agreement with our simulation. Also, from observed seasonal variations in the concentrations of GOM and PBM in the surface air and that of mercury deposited in the surface snow cover at Alert, Canada, Steffen et al. (2013b) found that the highest deposition of atmospheric mercury occurred when a major shift in the partitioning of oxidized mercury took place from PBM to RGM in May. Our model prediction is consistent with their finding at least qualitatively in that the deposition of GOM is a major source of mercury entering the surface snow. In this study, wet deposition is ignored for all the chemical species, but changes in the GOM-PBM partitioning can also make a difference in the wet deposition rate of oxidized mercury (e.g., Douglas et al., 2008; Amos et al., 2012). Considering relatively long lifetime against dry deposition, PBM contained in the sub-μm aerosols will be lost from the atmosphere primarily via wet deposition happening episodically. However, our skills are still premature in simulating precipitation processes and their impacts on wet deposition of aerosols and

ACPD
13, 22151–22220, 2013

gases in the polar region (Inoue et al., 2006; Korhonen et al., 2008; Shindell et al., 2008).

From six years of observations (1980 to 1986) at Alert, Barrie and Barrie (1990) showed the concentrations of "filterable bromine" to peak sharply from late March to early April. Although it has not been investigated deliberately, this seasonality may have shifted forward in recent decades (cf. Cole and Steffen, 2010). Anyhow, if indeed particulate bromide plays a major role in the GOM-PBM partitioning as simulated in our model, seasonal trends in the particulate bromide concentration may provide one explanation for the observed increase in RGM-to-PBM ratio at Alert in May (Steffen et al., 2013b). In addition, thermodynamic constants adopted in our chemical scheme are consonant with observed temperature trends in the RGM-PBM ratio. Figure 6a shows changes in simulated GOM-PBM partitioning with temperature assumed for the calculations of Henry's law for GOM species and aqueous-phase stability constants for Hg(II)-ligands in the atmospheric aerosols as well as in the LLL of the snow. If 268 K is assumed, instead of 253 K, for temperature in calculating the Hg(II) partitioning between gas- and aqueous-phases, the simulated build-up of PBM after the maturity of AMDEs is suppressed by a factor of four. If we assume 298 K, the simulated levels of PBM become negligibly small and thus GOM is always a dominant component of Hg(II) formed via GEM oxidation in the ABL. At Alert, median air temperatures are 248 K and 267 K, respectively, when PBM dominates RGM and vice versa (Steffen et al., 2013b). We note that, even at the temperature of 253 K, GOM dominates the simulated partitioning of oxidized mercury in our model while the concentrations of particulate bromide are maintained at low levels via multiphase recycling. Therefore, in order to provide a satisfactory explanation for seasonality in the GOM-PBM partitioning at Alert on the basis of our proposed mechanism, it is also required to assume a non-locality of AMDEs, in that the oxidation of GEM via bromine radical chemistry has terminated by the time air masses arrive at Alert, until mid April when PBM has been observed to dominate the partitioning almost all the time (Cobbett et al., 2007; Steffen et al., 2013b). A study by Bottenheim and Chan (2006) appears to support the prevalence of

ACPD
13, 22151–22220, 2013

distant origins of reactive halogens causing ODEs and AMDEs at Alert; by analyzing the cluster of 10-day backward trajectories of air masses arriving at Alert over 9 yr, these authors suggested that a majority of ODEs at Alert could have been initiated several days back in time over sea ice upwind across the central Arctic Ocean.

There is an indication that the apparent dry deposition velocities of GOM over the snow surface also depend on temperature. Figure 6b shows changes in the total vertical fluxes of GOM and PBM at the bottom of the atmosphere between the same model runs as discussed above. Obviously, the apparent dry deposition velocity of GOM is halved by raising temperature from 253 to 298 K for the calculations of thermodynamic constants related to the Hg(II) partitioning between the SIA and the LLL in the snowpack. We note, however, that the design of this experiment is not good enough to discuss the issue any further. For example, in these model runs, we did not account for changes in the LLL thickness on the snow grains with temperature and impurity concentrations (Döppenschmidt and Butt, 2000; Cho et al., 2002). Also ignored was a pivotal role of snowmelt near the melting point of water in flushing the impurities out of snowpack (e.g., Dommergue et al., 2003). It is beyond our present scope, but a better understanding of dry deposition of GOM on the snow surface may be pursued by handling these processes carefully in model calculations similar to ours.

3.4 Uncertainty in the gas-phase mechanism of mercury oxidation

Even with uncertainties in gas-phase kinetics, there is almost no doubt that bromine chemistry is critically involved in the oxidation of GEM during AMDEs (Calvert and Lindberg, 2004; Dastoor et al., 2008; Xie et al., 2008; Holmes et al., 2010; Subir et al., 2011; Stephens et al., 2012). But, if we are to advance our skills in predicting the location and magnitude of oxidized mercury depositing from the atmosphere during AMDEs, a better understanding of mechanisms for reactive halogen release is required in the first place (Abbatt et al., 2012, and references therein). For example, one of our objectives to develop the PHANTAS model was to give new insights into what may be happening inside the polar snowpack when it releases reactive bromine to

ACPD
13, 22151–22220, 2013

the atmosphere (Toyota et al., 2013). We also need a full identification of reactants involved in the GEM oxidation with a better quantification of rate coefficient for each step of elementary reactions.

As mentioned in the introduction, gas-phase oxidation of GEM initiated via reaction with Br-atoms involves a series of elementary steps competing each other before ending up with thermally stable products such as $HgBr_2$ (Calvert and Lindberg, 2004; Goodsite et al., 2004, 2012). As reviewed by Subir et al. (2011), two different methods, i.e., the transition state theory (TST) and the Rice-Ramsberger-Kassel-Markus (RRKM) theory, have been employed to approximate the dynamics of these reactions at the quantum level (e.g., Khalizov et al., 2003; Goodsite et al., 2004, 2012; Balabanov et al., 2005; Shepler et al., 2007), but rate constants estimated by both methods are subject to some level of uncertainty. A few laboratory studies measured the rate constants of *net* oxidation of GEM initiated via Br-attack (e.g., Ariya et al., 2002). Unfortunately, their applicability would be limited to the environment with reactant concentrations similar to those in the experimental system and at room temperature where the experiments were conducted. The rate constant of R1, adopted from a laboratory study by Donohoue et al. (2006) for our model runs, was exceptional in this sense, as the experiment was designed to measure the reaction rate of this elementary step itself. Of course, this rate constant is also subject to potential errors associated with methodological uncertainty (Subir et al., 2011). Hence, for the simulation of GEM oxidation via bromine radical chemistry in the gas phase, modelers must presently choose one of the following options: (1) lumping the whole reaction steps to a single net reaction while scaling down a laboratory-determined rate constant of the net reaction, or (2) resolving each of elementary reaction steps but in most cases using theoretically estimated rate constants. Here we chose the latter.

One of the major assumptions in our scheme of mercury chemistry is the feasibility of Reaction (R5). Our choice is based on a box model study by Calvert and Lindberg (2004) in which the rate constant of HgBr + BrO (Reaction R5) was simply assumed to be the same as that of HgBr + Br (Reaction R3). Although recent theoretical cal-

ACPD
13, 22151–22220, 2013

culations of bond energies support the viability of Reaction (R5) (Dibble et al., 2012), its rate constant adopted in our model is still considered to be highly uncertain. As a lucid test of this problem, we examined a sensitivity of simulated concentrations of GEM, GOM and PBM on Reaction (R5) by switching this reaction off (Fig. 7a–c). In this case, a further oxidation of HgBr (i.e., an initial product of Br-attack on GEM) is accomplished solely by the next attack by Br-atom, whose concentrations are generally lower by an order of magnitude or more than those of BrO radical (Fig. 8a). Consequently, a larger fraction of HgBr dissociates back to Hg and Br via Reaction (R2), dropping the net rate of GEM oxidation (Fig. 8b–c). At the height of 1.5 m above the snow surface, the lowest mixing ratios of GEM simulated in 8-day model runs at $U_2 = 2.0 \sim 8.5\,\mathrm{m\,s^{-1}}$ are $0.095 \sim 0.142\,\mathrm{pmol\,mol^{-1}}$ without Reaction (R5), as compared to $0.014 \sim 0.047\,\mathrm{pmol\,mol^{-1}}$ in base runs with Reaction (R5). Maximum dips from the background (initial) level of GEM ($0.168\,\mathrm{pmol\,mol^{-1}}$ assumed in this study) are therefore $0.121 \sim 0.154\,\mathrm{pmol\,mol^{-1}}$ and $0.026 \sim 0.073\,\mathrm{pmol\,mol^{-1}}$ with and without Reaction (R5), respectively. Although the total amounts of GEM oxidized and GOM produced become notably smaller by neglecting Reaction (R5), the build-up of PBM is not suppressed as much and in some cases even greater than in the base runs (Fig. 7a–c). As discussed later, in the model runs without Reaction (R5), a major acceleration occurs in net GEM oxidation when the concentrations of Br-atom ramp up concurrently with a shift in the GOM-PBM partitioning from GOM to PBM.

According to working definitions by Steffen et al. (2002) and Cole and Steffen (2010), GEM concentrations below $\sim 1\,\mathrm{ng\,m^{-3}}$ (or $\sim 0.12\,\mathrm{pmol\,mol^{-1}}$) are considered to be under the category of AMDEs. In our model runs, the lowest GEM levels simulated in the ABL do not always meet this criterion unless accounting for Reaction (R5) in the chemical scheme. Here we note that temperature dependence in the gas-phase kinetics of Reaction (R2) is presumably among the most influential to the net oxidation rate of GEM via reactions initiated by Br-attack (Goodsite et al., 2004). This is indicated also from our estimated changes in the net oxidation rate of GEM with temperature between 238 ~ 268 K using simulated concentrations of reactants at 253 K (Fig. 8b–c).

ACPD
13, 22151–22220, 2013

But, at the air temperature of 253 K assumed in our model runs, AMDEs are expected to occur nearly as often as ODEs (Tarasick and Bottenheim, 2002; Gauchard et al., 2005; Brooks et al., 2008; Cole and Steffen, 2010).

Goodsite et al. (2004) suggested that the reactions of HgBr with OH-radical, I-atom and Br-atom are all viable pathways for the formation of thermally stable GOM. In our model runs, however, the concentrations of OH-radical are probably too low (Fig. 8a), as compared to those of Br-atom, to make a difference in the net oxidation rate of GEM. In the Antarctic ABL over the frozen ocean, inorganic iodine from unknown sources can lead to the concentrations of I-atom even higher than those of Br-atoms, making the reaction HgBr + I one of the major potential routes to the formation of stable GOM (Saiz-Lopez et al., 2008). Even in the Arctic ABL where evidence suggests relatively low concentrations of I-atom as compared to the Southern Ocean ABL, this reaction might be as important as Reaction (R3) under some circumstances (Calvert and Lindberg, 2004). We do not address this issue here, as our model scheme does not contain iodine chemistry.

The theoretical calculations of bond energies for the products of the HgBr + X reactions indicate NO_2 and HO_2 perhaps as viable as BrO to form thermally stable GOM in the atmosphere (Dibble et al., 2012). In our model runs, the atmospheric concentrations of HO_2-radical are on the same order as those of Br-atom (Fig. 8a). Hence, HO_2 appears to be a fairly strong candidate that can enhance the net oxidation rate of GEM, but probably not as much as BrO (Fig. 8d). In the SIA, as a result of the release of NO_x and HONO via NO_3^- photolysis on the snow grains, chances are high that the mixing ratios of NO_2 exceed those of BrO (e.g., Peterson and Honrath, 2001). This is the case in our model runs where the NO_2 mixing ratios in the SIA are similar to and sometimes well in excess of BrO mixing ratios (Fig. 9a). If indeed NO_2 is as reactive as Br and/or BrO towards HgBr, NO_2 is a strong candidate that can enhance the net oxidation rate of GEM in the SIA (Fig. 9b–d).

There are yet other possibilities that can raise the rates of net GEM oxidation in the model. For example, if the rate constant of Reaction (R1) is actually closer to one of

ACPD
13, 22151–22220, 2013

the theoretical estimates (e.g., Shepler et al., 2007) than that adopted here from an experimental study by Donohoue et al. (2006), the rates of net GEM oxidation can be a factor of two (or more) greater than simulated in our model. It is also puzzling that the rate constant of Reaction (R1) determined by Donohoue et al. (2006) was significantly lower than those of net GEM oxidation initiated via Reaction (R1) as reported from other laboratory studies (Ariya et al., 2002; Subir et al., 2011). Products of GEM oxidation are often found to be adsorbed and/or aggregated as clusters on the surface of reaction vessels rather than identified in the gas phase, indicating that a part or all of the reactions may have been mediated heterogeneously by "wall effects" (Subir et al., 2011, and references therein). The type of surfaces conducive to the "wall effects" and their reaction mechanism(s) have not been fully elucidated yet. However, it will not be very surprising if redox reactions of mercury turn out to be mediated heterogeneously on various environmental surfaces (aerosols, vegetation, etc.) to a degree that they can change the overall rates of the reactions in many parts of the atmosphere (Subir et al., 2012). It was beyond our scope to study the surface adsorption of mercury compounds and their potential reactions, but they might indeed play a role especially in the SIA because of high surface-to-volume ratios.

Kinetics of gas-phase bromine chemistry leading to ozone loss is now well understood and constrained extensively by laboratory experiments (e.g., Atkinson et al., 2007). Hence, for given concentrations of bromine radicals, the net photochemical loss rates of ozone can be estimated with greater confidence than the net oxidation rates of GEM. Scatter plots of data between the concentrations of total gaseous mercury (GEM + GOM) and ozone can thus serve as an alternative means to test the realism of our reaction mechanism for mercury. In our base runs with Reaction (R5), the concentrations of total gaseous mercury and ozone (at the height of 1.5 m in the air) exhibit a compact linear relationship (Fig. 10a). This correlation becomes slightly disturbed if we assume the "fast" photo-reduction of Hg(II) in the snowpack to accelerate the recovering of GEM after the maturity of AMDEs (Fig. 10b). If, by neglecting Reaction (R5), Br-atom is assumed to be the only reactant supporting the formation of

ACPD
13, 22151–22220, 2013

GOM, the relationship becomes non-linear in that the rate of net GEM oxidation is accelerated as ozone is depleted to sufficiently low levels (Fig. 10c). It should be noted that the trends simulated in our model of Br-atom concentrations increasing particularly below 10 nmol mol^{-1} of ozone are consistent with evidence in the field (Toyota et al., 2013, Sect. 3.2). The scatter plots of the same kind have been created by using field data obtained in the polar regions from both hemispheres, showing roughly linear relationships between the mercury and ozone concentrations (Schroeder et al., 1998; Ebinghaus et al., 2002); although not conclusively, the field data appear to favor the scenario of Reaction (R5) operating effectively during the AMDEs as simulated here. Comparison between models and observations using such scatter plots will be more compelling if it is done with a 3-D model simulating the transport of bromine, ozone and mercury and their chemical interactions altogether (e.g., Holmes et al., 2010).

3.5 Relationship between BrO columns and the deposition of oxidized mercury in the ABL

In our base runs with Reaction (R5) in the chemical scheme, the model predicts a compact linear relationship between the "daytime" (5–19 h in local solar time) mean of atmospheric BrO columns and the daily mean of total depositional fluxes of GOM and PBM (Fig. 11a). As discussed earlier, the net oxidation of GEM is facilitated strongly via Reaction (R5) if it is included in the model. While BrO maintains high levels in the ABL, the accumulation of bromide in sub-μm aerosols is kept minimal and thus our model predicts GOM dominating PBM in the partitioning of oxidized mercury. Dry deposition of GOM takes place rapidly enough to accomplish a near-complete loss of the oxidized mercury products from the atmosphere on the timescale of a day. The high correlation (r^2 = 0.96) between BrO columns and the depositional fluxes of GOM + PBM is also a consequence of simulated trends of atmospheric BrO column increasing with the ABL thickness (Toyota et al., 2013, see Sect. 3.4). When integrated over the atmospheric column, the amount of mercury oxidized and then deposited tends to be greater as the

ACPD
13, 22151–22220, 2013

ABL gets deeper in response to increased surface wind assumed for diagnosing the profiles of turbulent diffusivity.

The relationship between BrO columns and the deposition of GOM + PBM becomes quite scattered if Reaction (R5) is switched off in the chemical scheme (Fig. 11b). In this scenario of mercury chemistry, the simulated rate of net GEM oxidation does not maximize when BrO reaches its highest levels over time, because temporal trends in the mixing ratios of BrO and Br-atom are not coherent perfectly (Fig. 8a). Nonetheless, there is still a modest correlation ($r^2 = 0.37$) between BrO columns and the deposition of GOM + PBM because, on the timescale of a whole progress of AMDEs/ODEs, the mixing ratios of BrO and Br-atom are more or less correlated. Also, the relationship between the ABL thickness and the total column amount of mercury being oxidized/deposited holds as in the case of base runs.

It remains a challenge to assign the source strength of reactive bromine correctly across different domains of the troposphere, in particular for natural processes such as those involving saline ice surfaces and sea-salt aerosols, in 3-D models (e.g., Theys et al., 2011; Toyota et al., 2011; Parrella et al., 2012). Therefore, if one wishes to assess the deposition of mercury from the polar boundary layer by a 3-D model, it can be useful to begin with BrO column data retrieved from satellite as external constraint for the simulation of AMDEs (e.g., Dastoor et al., 2008), as long as the satellite data are carefully processed to screen out BrO residing above the ABL (e.g., Theys et al., 2011; Sihler et al., 2012) and the concentrations of Br-atom are estimated reasonably well from those of BrO by exploiting some ancillary data to calculate the Br/BrO ratios (e.g., Zeng et al., 2006).

3.6 In-snow behaviors of mercury after its deposition

Figure 12a–e shows the temporal evolution of total dissolved mercury (THg) and its speciation in the LLL in each of the top six layers (0 ~ 3 cm depth) of snowpack as simulated at $U_2 = 4.5\,\mathrm{m\,s^{-1}}$. Our model predicts that a vast majority of GOM entering the snowpack from the atmosphere is taken up by snow grains within the top 1-mm

ACPD
13, 22151–22220, 2013

layer. Until Day 4, a rapid increase in the THg loading (up to $\sim 80\,ng\,L^{-1}$) occurs in this top layer during the day, which parallels (with a short delay) changes in the dry depositional fluxes of GOM (Fig. 4b). The dry deposition of PBM has a minimal impact on the THg loading in the snowpack, as discussed in Sect. 3.3. The increase in the top-layer THg levels during the day is followed by a decrease at night as a result of vertical diffusion down through the LLL network with a smaller supply from the atmosphere. Underneath the top 1 mm layer, THg is sourced mostly via the vertical diffusion of oxidized mercury deposited from the atmosphere through the LLL network. However, this happens only within the top several centimeters of snowpack during the 8-day time span of our model run (Fig. 13a). THg builds up obviously at lower rates below the top 1 mm layer. But, within the top 2 cm layer, the delay in the THg build-up is on the order of a few days only. Changes in the mean concentrations of THg in the top 3 cm layer of snowpack are represented well by an average between the depth of $0.1 \sim 2$ cm (Fig. 12f). Further below, the photo-oxidation of GEM in the SIA is a major source of THg (see Sect. 3.2), but it only results in the marginal loading of THg up to the order of $0.1\,ng\,L^{-1}$ over 8 days (Fig. 13a).

If the vertical diffusion through the LLL network is switched off, the model predicts that up to around $1000\,ng\,L^{-1}$ of THg can accumulate in the top 1 mm layer of snowpack (Fig. 13b). On the other hand, below the depth of 1 cm, the THg levels never exceed $0.1\,ng\,L^{-1}$ over 8 days. Douglas et al. (2005) measured dissolved mercury concentrations in frost flowers, hoar frost and "reference snow" along sea ice leads sampled near Barrow in the springs of 2003 and 2004. In one sample of surface hoar with an estimated age of ~ 11 days, they measured $820\,ng\,L^{-1}$ of mercury, as compared to $91\,ng\,L^{-1}$ found in the reference snow sampled nearby. This observation might indicate a possibility that mercury deposited from the atmosphere can stay in a very thin layer on the top of snowpack without migrating much into the bulk of underlying snowpack over 10 days or so. However, hoar frost itself is formed and grows by the condensation of water vapor and thus deposited mercury might be occluded inside the ice structure

ACPD
13, 22151–22220, 2013

via burial uptake (Douglas and Sturm, 2004). If this occurs, the deposited mercury would be indeed much less mobile than in the LLL (Asaduzzaman et al., 2012).

Simulated speciation of THg is dominated by $HgCl_4^{2-}$, $HgCl_3Br^{2-}$ and $HgCl_2Br_2^{2-}$ (Fig. 12a–f). Concentration ratios between these major species exhibit notable variations with time especially in the top 1 mm layer, in response to changes in bromide concentrations via multiphase photochemical processing (Toyota et al., 2013, see Fig. 6, bottom row). The initial molar ratio between bromide and chloride in the LLL was assumed to be the same as that in seawater (= 1/650, Millero et al., 2008). Our model ignores wind-blown snow (Jones et al., 2009) and its sublimated residues (or sea-salt aerosols) (Yang et al., 2008) over the frozen ocean, but, if it did, the speciation of Hg(II) in these atmospheric particles would be not very different from what is simulated in the LLL of our snowpack. In the wind-blown snow particles sampled at Barrow, Brooks et al. (2008) measured as high as $\sim 500\,ng\,L^{-1}$ of mercury. To our knowledge, atmospheric models have not considered a possibility of producing mixed-halide Hg(II) complexes in deliquesced (aqueous) aerosols and in cloud/rain water. However, for the study of Hg(II) speciation in seawater, there have been a few thermodynamic models in which the formation of mixed-halide Hg(II) complexes is taken into account. For example, Dyrssen and Wedborg (1980), as cited in Lindqvist and Rodhe (1985), estimated that ca. 18 % of inorganic Hg(II) in seawater would exist as mixed Hg(II)-chloride-bromide compounds ($HgCl_3Br^{2-}$, $HgCl_2Br^-$ and HgClBr).

Here we note that the role of dissolved organic matter is ignored in our chemical scheme. Hg(II)-(organo-)sulfur complexes formed via interactions with humic materials can dominate the Hg(II) speciation in terrestrial and estuarine waters, but this is rather unlikely to be the case in the ocean if it is far from the coast (e.g., Mantoura et al., 1978). Hence, even if the humic materials are rejected from freezing seawater into brine along with inorganic solutes (e.g., Giannelli et al., 2001), the fraction of organically-bound Hg(II) in brine-laid sea ice and overlying snowpack is expected to be smaller than the fraction bound to chloride and bromide (Mantoura et al., 1978). Observational evidence, however, suggests that biological activities can create (and also

ACPD
13, 22151–22220, 2013

consume) dissolved organic carbon in the sea ice (Thomas et al., 2001). This leaves some possibility that a fraction of Hg(II) is bound to organic matters not only in the terrestrial snow cover but also in the snowpack on land-fast ice and even on pelagic sea ice.

Figure 14 shows changes in the build-up rate of THg in the top 3 cm of snowpack from eight model runs (at four different wind speeds and with two different in-snow Hg(II) photo-reduction scenarios). As noted in Sect. 3.5, the deposition of oxidized mercury from the atmosphere is simulated to increase with the diagnosed ABL thickness, which in turn increases with surface wind speed assumed for our meteorological calculations (Toyota et al., 2013, see Sect. 2.7). At $U_2 = 2.0\,\mathrm{m\,s^{-1}}$ where the ABL thickness never exceeds 44 m, THg levels accumulating in the top 3 cm snowpack do not exceed $4\,\mathrm{ng\,L^{-1}}$ over the course of simulated AMDEs. At higher wind speeds ($U_2 = 4.5 \sim 12.0\,\mathrm{m\,s^{-1}}$) and hence with greater ABL thickness (119 ∼ 429 m), the top 3 cm snow accumulates up to $12 \sim 50\,\mathrm{ng\,L^{-1}}$ of THg at some point of each model run over 8 days. All of these simulated rates of increase in the snowpack THg levels drop significantly or are even reversed to decreasing trends, once the partitioning of oxidized mercury in the ABL is shifted from GOM to PBM. This gives an explanation for apparent connection between mercury levels in the surface snow and the depletion of mercury in the surface air sometimes found and at other times not (Durnford and Dastoor, 2011, and references therein).

4 Conclusions

To study the physical and chemical processes involved in reactive bromine release and its impacts on AMDEs and ODEs in the springtime Arctic, we have developed PHANTAS, a 1-D model that simulates multiphase chemistry and transport of trace constituents throughout porous snowpack and in the overlying ABL. A common set of reactions are employed to describe multiphase chemistry of a gas-aerosol system in the atmosphere and of a gas-brine system in the snowpack. Building on a study

ACPD
13, 22151–22220, 2013

reported in the companion paper on in-snow bromine activation and its two-way interactions with ozone (Toyota et al., 2013), this paper is focused on processes related to AMDEs. For the chemical mechanism of mercury, we incorporated an explicit description of each elementary step involved in the net oxidation of GEM to GOM with temperature-dependent rate coefficients adopted from the literature. Also, for a description of the gas-aerosol and gas-LLL partitioning of Hg(II) species, we used Henry's law for GOM and thermodynamic equilibrium constants for the ligands of Hg(II) with chloride (Cl^-), bromide (Br^-) and hydroxyl (OH^-) in the aqueous phase (sulfate aerosols in the air and the LLL in the snowpack) with temperature dependence adopted directly from the literature and/or estimated from reference thermodynamic data.

Analysis of our model runs indicates that, during AMDEs, BrO radical would likely accelerate the net oxidation of GEM in the gas phase via reaction with HgBr, which is a thermally unstable initial product formed via the reaction Hg + Br. The timing of major GEM oxidation during the concurrent progress of AMDEs and ODEs was shown to depend strongly on whether or not the reaction HgBr + BrO is viable under atmospheric conditions and proceeds at sufficiently fast rates. In the SIA, NO_2 might also play a key role in the formation of a thermally stable oxidized mercury via the reaction HgBr + NO_2. On the basis of theoretical calculations of bond energies, Dibble et al. (2012) indicated the viability of these reactions under atmospheric conditions. However, their rate constants have been unexplored theoretically and experimentally and hence are recommended to be studied in the future.

The gas-aerosol partitioning of oxidized mercury was predicted to be sensitive to bromide content in the aerosols. According to model calculations (e.g., Sander et al., 1997; Toyota et al., 2013), in the springtime Arctic, high concentrations of particulate bromide are encountered especially in air masses where ozone is significantly depleted. While in the build-up stage of reactive bromine in the ABL with relatively high concentrations of ozone, multiphase recycling occurs very actively to maintain the concentrations of particulate bromide to minimal levels. At this point, a vast majority of oxidized mercury stays in the gas phase as GOM. Only when particulate bromide starts building up in the

ACPD
13, 22151–22220, 2013

air, GOM becomes susceptible to an uptake to the aerosols to form PBM. Here, $HgBr_4^{2-}$ constitutes a dominant fraction of PBM in our model runs. Owing to temperature dependence of the estimated thermodynamic constants, the build-up of PBM is predicted to be suppressed significantly by raising temperature from 253 to 268 K for calculating Henry's law of Hg(II) species and equilibria between the ligands in the model. This appears to be consistent, at least qualitatively, with temperature dependence in the observed GOM-PBM partitioning at Alert (Cobbett et al., 2007; Steffen et al., 2013b). We used reference thermochemical data from Wagman et al. (1982) and Hepler and Olofsson (1975) to derive thermodynamic constants and their temperature dependence for the simulation of GOM-PBM partitioning. But these constants should be re-examined experimentally.

Sulfate aerosols prevailing in the Arctic Haze are too acidic (Li, 1994; Staebler et al., 1999) to build up particulate chloride via uptake of gaseous HCl. On the other hand, if PBM is formed in deliquesced sea-salt aerosols (currently ignored in our model), its speciation patterns would be similar to what was simulated in the LLL of our modeled snowpack, perhaps dominated by $HgCl_4^{2-}$, $HgCl_3Br^{2-}$ and $HgCl_2Br_2^{2-}$ (cf. Holmes et al., 2009). We note, however, that, in a study of the GOM-PBM partitioning using observational data at Alert, Steffen et al. (2013b) suggested sea-salt aerosols to be of secondary importance because they were not so abundant as sulfate aerosols.

During field measurements of speciated mercury, ozone and BrO in the surface air on sea ice near Barrow in March 2009, temporal changes in the concentrations of GEM, PBM and ozone exhibited a linear relationship in that PBM built up when GEM and ozone were depleted, whereas the concentration of RGM was not correlated very well with any of them but with that of BrO (Steffen et al., 2013a). This observation gives a strong support to our present model results in the following two aspects: (1) PBM builds up via the aerosol uptake of GOM when particulate bromide levels increase as a result of ozone depletion in the air and (2) BrO is involved in the net oxidation of GEM during AMDEs. A caveat is that one field study at Ny Ålesund, Svalbard, indicated a persistence of relatively high particulate bromide levels regardless of ozone

ACPD
13, 22151–22220, 2013

concentrations in the air (Staebler et al., 1999). If actual factors controlling the atmospheric concentrations of particulate bromide are largely misrepresented in our model calculations, the GOM-PBM partitioning during AMDEs may be not as sensitive to the progress of concurrent ODEs as simulated in our model. This will be the case especially when particulate bromide is sourced via sublimation of wind-blown snow (Yang et al., 2008).

GOM was predicted to be very susceptible to dry deposition to the snow surface, in agreement with a field study of RGM vertical fluxes (Skov et al., 2006). Since the dry deposition of PBM (in the sub-μm size range) occurs much more slowly than that of GOM, PBM will not undergo the deposition from the atmosphere very soon after its formation unless scavenged by episodic precipitation. Therefore, a major input of oxidized mercury from the atmosphere to the snowpack (and, by extension, to the ecosystem) during AMDEs was simulated to take place by the deposition of GOM. This is consistent with some of the previous observational studies, which found a strong link between high levels of GOM in the surface air and the accumulation of deposited mercury in the surface snow in the springtime Arctic (Lindberg et al., 2002; Steffen et al., 2013b).

In summary, to predict the exact timing and magnitude of AMDEs and their impacts on the mercury loading in the polar snow cover, we will likely need also to predict the concurrent progress, along with the vertical structure, of ODEs and its impact on the partitioning of reactive bromine in the gas phase and bromide content in the aerosols correctly.

ACPD
13, 22151–22220, 2013

Appendix A

Thermodynamic equilibria for Hg(II)-halide complexes in the aqueous phase

The aqueous-phase equilibrium constant $K^{\ominus}$ at standard ambient temperature ($T^{\ominus}$ = 298.15 K) for a reversible reaction $A_1 + A_2 + \cdots \rightleftarrows B_1 + B_2 + \cdots$ is obtained by

$$K^{\ominus} = \frac{\prod[B_i]}{\prod[A_i]} = \exp\left(-\frac{\Delta G^{\ominus}}{RT^{\ominus}}\right) \quad \text{(A1)}$$

where $\Delta G^{\ominus}$ is a net change in the Gibbs free energy, i.e. $\sum \Delta G_f^{\ominus}(B_i) - \sum \Delta G_f^{\ominus}(A_i)$, and R is the gas constant. According to the van't Hoff equation, temperature dependence of the equilibrium constant can be expressed by using a net change in the standard enthalpy, $\Delta H^{\ominus} = \sum \Delta H_f^{\ominus}(B_i) - \sum \Delta H_f^{\ominus}(A_i)$:

$$K(T) = K^{\ominus} \times \exp\left[\frac{-\Delta H^{\ominus}}{R}\left(\frac{1}{T} - \frac{1}{T^{\ominus}}\right)\right] \quad \text{(A2)}$$

In this study, we simulate the formation of coordination complexes of Hg(II) with chloride, bromide and hydroxyl anions in aerosols and in the brine layer of snowpack. In the case of coordination complexes formed with a single type of anions (e.g., $HgCl_4^{2-}$, $HgCl_3^{-}$), $K(T)$ can be calculated simply by using the values of $\Delta G_f^{\ominus}$ and $\Delta H_f^{\ominus}$ available from a critical review on the thermochemical constants of mercury compounds by Hepler and Olofsson (1975) and a comprehensive thermochemical table compiled by Wagman et al. (1982).

For mixed-ligand formation such as in the Hg(II)-chloride-bromide system, we employ an empirical approach proposed by Marcus and Eliezer (1962) and Spiro and Hume (1963). For example, exchange between Cl^- and Br^- in a saturated, tetrahedral coordination, consisting of four halide anions around Hg^{2+}, will proceed in the following stoichiometry:

$$HgCl_4^{2-} + n\,Br^- \rightleftarrows HgCl_{4-n}Br_n^{2-} + n\,Cl^- \quad (n = 1 \sim 4)$$

ACPD
13, 22151–22220, 2013

The calculation of the equilibrium constant for each step of this halide exchange begins with looking at changes in free energy by total replacement:

$$HgCl_4^{2-} + 4\,Br^- \rightleftarrows HgBr_4^{2-} + 4\,Cl^-$$

where the $\Delta G_f^{\ominus}$ and $\Delta H_f^{\ominus}$ values for each species in this reaction are taken from from Hepler and Olofsson (1975) and/or Wagman et al. (1982). This free energy change is divided equally between the successive replacement steps and then a contribution from an entropy change arising from the mixing of the ligands ("statistical effect") is added. These procedures end up in the following formulation:

$$\log \gamma_n = \frac{n}{4} \log \gamma_4 + \log \frac{4!}{(4-n)!\,n!} \tag{A3}$$

where

$$\gamma_n = \frac{[HgCl_{4-n}Br_n^{2-}][Cl^-]^n}{[HgCl_4^{2-}][Br^-]^n}$$

Note that the second term in the right-hand side of Eq. (A3) represents the "statistical effect" and is independent of temperature. But, γ_4 calculated by Eq. (A2) is dependent on temperature, so is γ_n. Dyrssen and Wedborg (1980) estimated the speciation of inorganic Hg(II) in seawater, based on Eq. (A3) for the stability constants of mixed-chloride-bromide Hg(II) complexes at 25 °C.

According to Marcus and Eliezer (1962) and Spiro and Hume (1963), the γ_n values thus calculated should be adjusted further by an "electrostatic effect" arising from coulombic repulsion and polarization between different ligands:

$$\log \gamma_n = \frac{n}{4} \log \gamma_4 + \log \frac{4!}{(4-n)!\,n!} + \log \frac{\Delta E_{el}}{k_b T} \tag{A4}$$

where ΔE_{el} is a difference between $HgCl_{4-n}Br_n^{2-}$ and $HgCl_4^{2-}$ in the electrostatic energy of coulombic interactions inside the molecules and k_b is the Boltzmann constant.

ACPD
13, 22151–22220, 2013

Details on the calculation of ΔE_{el} can be found in Marcus and Eliezer (1962). The example above describes the case with saturated (tetrahedral) coordination, but unsaturated complexes such as $HgCl_2Br^-$ and HgClBr can be dealt with by the same approach (Marcus and Eliezer, 1962). In this study, we use Eq. (A4) (or its variant forms for the unsaturated complexes) to calculate the equilibrium constants associated with the mixed-chloride-bromide Hg(II) complex formation.

Acknowledgements. This study was supported by funding from the Clean Air Regulatory Agenda (CARA) at Environment Canada. We wish to thank M. Subir, A. Steffen, G. Kos, P. A. Ariya and F. Wang for useful discussion on mercury chemistry and measurements.

References

Abbatt, J. P. D., Thomas, J. L., Abrahamsson, K., Boxe, C., Granfors, A., Jones, A. E., King, M. D., Saiz-Lopez, A., Shepson, P. B., Sodeau, J., Toohey, D. W., Toubin, C., von Glasow, R., Wren, S. N., and Yang, X.: Halogen activation via interactions with environmental ice and snow in the polar lower troposphere and other regions, Atmos. Chem. Phys., 12, 6237–6271, doi:10.5194/acp-12-6237-2012, 2012. 22157, 22162, 22174

Albert, M. R. and Shultz, E. F.: Snow and firn properties and air-snow transport processes at Summit, Greenland, Atmos. Environ., 36, 2789–2797, 2002. 22160

Allard, B. and Arsenie, I.: Abiotic reduction of mercury by humic substances in aquatic system – an important process for the mercury cycle, Water Air Soil Pollut., 56, 457–464, 1991. 22163

AMAP: AMAP Assessment 2011: Mercury in the Arctic, Arctic Monitoring and Assessment Programme (AMAP), Oslo, Norway, 2011. 22154

Amos, H. M., Jacob, D. J., Holmes, C. D., Fisher, J. A., Wang, Q., Yantosca, R. M., Corbitt, E. S., Galarneau, E., Rutter, A. P., Gustin, M. S., Steffen, A., Schauer, J. J., Graydon, J. A., St. Louis, V. L., Talbot, R. W., Edgerton, E. S., Zhang, Y., and Sunderland, E. M.: Gas-particle partitioning of atmospheric Hg(II) and its effect on global mercury deposition, Atmos. Chem. Phys., 12, 591–603, doi:10.5194/acp-12-591-2012, 2012. 22157, 22171, 22172

Andersson, M. E., Gårdfeldt, K., Wängberg, I., and Strömberg, D.: Determination of Henry's law constant for elemental mercury, Chemosphere, 73, 587–592, 2008. 22163

ACPD
13, 22151–22220, 2013

Ariya, P. A., Khalizov, A., and Gidas, A.: Reactions of gaseous mercury with atomic and molecular halogens: kinetics, product studies, and atmospheric implications, J. Phys. Chem. A, 106, 7310–7320, 2002. 22156, 22175, 22178

Ariya, P. A., Dastoor, A. P., Amyot, M., Schroeder, W. H., Barrie, L., Anlauf, K., Raofie, F., Ryzhkov, A., Davignon, D., Lalonde, J., and Steffen, A.: The Arctic: a sink for mercury, Tellus, 56B, 397–403, 2004. 22154, 22155

Asaduzzaman, A., Wang, F., and Schreckenbach, G.: Quantum-chemical Study of the diffusion of Hg(0, I, II) into the Ice(Ih), J. Phys. Chem., 116, 5151–5154, 2012. 22159, 22182

Aspmo, K., Temme, C., Berg, T., Ferrari, C., Gauchard, P.-A., Fain, X., and Wibetoe, G.: Mercury in the Atmosphere, Snow and Melt Water Ponds in the North Atlantic Ocean during Arctic Summer, Environ. Sci. Technol., 40, 4083–4089, 2006. 22155, 22171

Atkinson, R., Baulch, D. L., Cox, R. A., Crowley, J. N., Hampson, R. F., Hynes, R. G., Jenkin, M. E., Rossi, M. J., and Troe, J.: Evaluated kinetic and photochemical data for atmospheric chemistry: Volume III – gas phase reactions of inorganic halogens, Atmos. Chem. Phys., 7, 981–1191, doi:10.5194/acp-7-981-2007, 2007. 22178

Balabanov, N. B., Shepler, B. C., and Peterson, K. A.: Accurate global potential energy surface and reaction dynamics for the ground state of $HgBr_2$, J. Phys. Chem. A, 109, 8765–8773, 2005. 22156, 22175, 22206

Banic, C. M., Beauchamp, S. T., Tordon, R. J., Schroeder, W. H., Steffen, A., Anlauf, K. A., and Wong, H. K. T.: Vertical distribution of gaseous elemental mercury in Canada, J. Geophys. Res., 108, 4264, doi:10.1029/2002JD002116, 2003. 22166

Barret, M., Domine, F., Houdier, S., Gallet, J.-C., Weibring, P., Walega, J., Fried, A., and Richter, D.: Formaldehyde in the Alaskan Arctic snowpack: Partitioning and physical processes involved in air-snow exchanges, J. Geophys. Res., 116, D00R03, doi:10.1029/2011JD016038, 2011. 22159

Barrie, L. A. and Barrie, M. J.: Chemical components of lower tropospheric aerosols in the high Arctic: Six years of observations, J. Atmos. Chem., 11, 211–226, 1990. 22173

Barrie, L. A., Bottenheim, J. W., Schnell, R. C., Crutzen, P. J., and Rasmussen, R. A.: Ozone destruction and photochemical reactions at polar sunrise in the lower Arctic troposphere, Nature, 334, 138–141, 1988. 22167

Bartels-Rausch, T., le Krysztofiak, G.-C., Bernhard, A., Schläppi, M., Schwikowski, M., and Ammann, M.: Photoinduced reduction of divalent mercury in ice by organic matter, Chemosphere, 82, 199–203, 2011. 22163

ACPD
13, 22151–22220, 2013

Bottenheim, J. W. and Chan, E.: A trajectory study into the origin of spring time Arctic boundary layer ozone depletion, J. Geophys. Res., 111, D19301, doi:10.1029/2006JD007055, 2006. 22173

Brooks, S., Lindberg, S., Southworth, G., and Arimoto, R.: Springtime atmospheric mercury speciation in the McMurdo, Antarctica coastal region, Atmos. Environ., 42, 2885–2893, 2008. 22157, 22158, 22170, 22177, 22182

Brooks, S. B., Saiz-Lopez, A., Skov, H., Lindberg, S. E., Plane, J. M. C., and Goodsite, M. E.: The mass balance of mercury in the springtime arctic environment, Geophys. Res. Lett., 33, L13812, doi:10.1029/2005GL025525, 2006. 22154, 22157

Calvert, J. G. and Lindberg, S. E.: The potential influence of iodine-containing compounds on the chemistry of the troposphere in the polar spring. II. Mercury depletion, Atmos. Environ., 38, 5105–5116, 2004. 22156, 22162, 22163, 22168, 22174, 22175, 22177, 22206

Calvert, J. G. and Lindberg, S. E.: Mechanisms of mercury removal by O_3 and OH in the atmosphere, Atmos. Environ., 39, 3355–3367, 2005. 22162

Cho, H., Shepson, P. B., Barrie, L. A., Cowin, J. P., and Zaveri, R.: NMR investigation of the quasi-brine layer in ice/brine mixtures, J. Phys. Chem. B, 106, 11226–11232, 2002. 22159, 22165, 22174

Cobbett, F. D., Steffen, A., Lawson, G., and Heyst, B. J. V.: GEM fluxes and atmospheric mercury concentrations (GEM, RGM and Hg^p) in the Canadian Arctic at Alert, Nunavut, Canada (February–June 2005), Atmos. Environ., 41, 6527–6543, 2007. 22157, 22158, 22171, 22173, 22185

Colbeck, S. C.: Grain Clusters in Wet Snow, J. Coll. Interf. Sci., 72, 371–384, 1979. 22160

Cole, A. S. and Steffen, A.: Trends in long-term gaseous mercury observations in the Arctic and effects of temperature and other atmospheric conditions, Atmos. Chem. Phys., 10, 4661–4672, doi:10.5194/acp-10-4661-2010, 2010. 22165, 22173, 22176, 22177

Cunningham, J. and Waddington, E. D.: Air flow and dry deposition of non-sea salt sulfate in polar firn: Paleoclimatic implications, Atmos. Environ., 27A, 2943–2956, 1993. 22160

Dastoor, A. P. and Larocque, Y.: Global circulation of atmospheric mercury: a modeling study, Atmos. Environ., 38, 147–161, 2004. 22162

Dastoor, A. P., Davingnon, D., Theys, N., Roozendael, M. V., Steffen, A., and Ariya, P. A.: Modeling dynamic exchange of gaseous elemental mercury at polar sunrise, Environ. Sci. Tech., 42, 5183–5188, 2008. 22154, 22155, 22157, 22162, 22163, 22174, 22180

ACPD
13, 22151–22220, 2013

Dibble, T. S., Zelie, M. J., and Mao, H.: Thermodynamics of reactions of ClHg and BrHg radicals with atmospherically abundant free radicals, Atmos. Chem. Phys., 12, 10271–10279, doi:10.5194/acp-12-10271-2012, 2012. 22168, 22176, 22177, 22184

Domine, F., Sparapani, R., Ianniello, A., and Beine, H. J.: The origin of sea salt in snow on Arctic sea ice and in coastal regions, Atmos. Chem. Phys., 4, 2259-2271, doi:10.5194/acp-4-2259-2004, 2004. 22160

Domine, F., Albert, M., Huthwelker, T., Jacobi, H.-W., Kokhanovsky, A. A., Lehning, M., Picard, G., and Simpson, W. R.: Snow physics as relevant to snow photochemistry, Atmos. Chem. Phys., 8, 171–208, doi:10.5194/acp-8-171-2008, 2008. 22160

Dommergue, A., Ferrari, C. P., Gauchard, P.-A., Boutron, C. F., Poissant, L., Pilote, M., Jitaru, P., and Adams, F.: The fate of mercury species in a sub-arctic snowpack during snowmelt, Geophys. Res. Lett., 30, 1621, doi:10.1029/2003GL017308, 2003. 22174

Dommergue, A., Bahlmann, E., Ebinghaus, R., Ferrari, C., and Boutron, C.: Laboratory simulation of Hg^0 emissions from a snowpack, Anal. Bioanal. Chem., 388, 319–327, 2007. 22164

Donohoue, D. L., Bauer, D., Cossairt, B., and Hynes, A. J.: Temperature and pressure dependent rate coefficients for the reaction of Hg with Br and the reaction of Br with Br: a pulsed laser photolysis-pulsed laser induced fluorescence study, J. Phys. Chem. A, 110, 6623–6632, 2006. 22155, 22162, 22175, 22178, 22206

Döppenschmidt, A. and Butt, H.-J.: Measuring Thickness of the Liquid-like Layer on Ice Surfaces with Atomic Force Microscopy, Langmuir, 16, 6709–6714, 2000. 22174

Douglas, T., Sturm, M., Simpson, W., Brooks, S., Lindberg, S., and Perovich, D.: Elevated mercury measured in snow and frost flowers near Arctic sea ice leads, Geophys. Res. Lett., 32, L04502, doi:10.1029/2004GL022132, 2005. 22181

Douglas, T. A. and Sturm, M.: Arctic haze, mercury and the chemical composition of snow across northwestern Alaska, Atmos. Environ., 38, 805–820, 2004. 22182

Douglas, T. A., Sturm, M., Simpson, W. R., Blum, J. D., Alvarez-Aviles, L., Keeler, G., Perovich, D., Biswas, A., and Johnson, K.: Influence of Snow and Ice Crystal Formation and Accumulation on Mercury Deposition to the Arctic, Environ. Sci. Technol., 42, 1542–1551, 2008. 22172

Durnford, D. and Dastoor, A.: The behavior of mercury in the cryosphere: A review of what we know from observations, J. Geophys. Res., 116, D06305, doi:10.1029/2010JD014809, 2011. 22164, 22183

ACPD
13, 22151–22220, 2013

Durnford, D., Dastoor, A., Ryzhkov, A., Poissant, L., Pilote, M., and Figueras-Nieto, D.: How relevant is the deposition of mercury onto snowpacks? – Part 2: A modeling study, Atmos. Chem. Phys., 12, 9251–9274, doi:10.5194/acp-12-9251-2012, 2012. 22155, 22171

Dyrssen, D. and Wedborg, M.: Major and minor elements, chemical speciation in estuarine waters, in: Chemistry and biochemistry of estuaries, edited by: Olausson, E. and Cato, I., John Wiley, Chichester, 1980. 22182, 22188

Ebinghaus, R., Kock, H. H., Temme, C., Einax, J. W., Lowe, A. G., Richter, A., Burrows, J. P., and Schroeder, W. H.: Antarctic springtime depletion of atmospheric mercury, Environ. Sci. Technol., 36, 1238–1244, 2002. 22168, 22179, 22216

Evans, M. J., Jacob, D. J., Atlas, E., Cantrell, C. A., Eisele, F., Flocke, F., Fried, A., Mauldin, R. L., Ridley, B. A., Wert, B., Talbot, R., Blake, D., Heikes, B., Snow, J., Walega, J., Weinheimer, A. J., and Dibb, J.: Coupled evolution of BrOx-ClOx-HOx-NOx chemistry during bromine-catalyzed ozone depletion events in the arctic boundary layer, J. Geophys. Res., 108, 8368, doi:10.1029/2002JD002732, 2003. 22166

Fain, X., Ferrari, C. P., Gauchard, P.-A., Magand, O., and Boutron, C.: Fast depletion of gaseous elemental mercury in the Kongsvegen Glacier snowpack in Svalbard, Geophys. Res. Lett., 33, L06826, doi:10.1029/2005GL025223, 2006. 22170

Faïn, X., Grangeon, S., Balhmann, E., Fritsche, J., Obrist, D., Dommergue, A., Ferrari, C., Cairns, W., Ebinghaus, R., Barbante, C., Cescon, P., and Boutron, C.: Diurnal production of gaseous mercury in the alpine snowpack before snowmelt, J. Geophys. Res., 112, D21311, doi:10.1029/2007JD008520, 2007. 22164

Ferrari, C. P., Dommergue, A., Boutron, C. F., Jitaru, P., and Adams, F. C.: Profiles of Mercury in the snow pack at Station Nord, Greenland shortly after polar sunrise, Geophys. Res. Lett., 31, L03401, doi:10.1029/2003GL018961, 2004. 22170

Ferrari, C. P., Gauchard, P.-A., Aspmo, K., Dommergue, A., Magand, O., Bahlmann, E., Nagorski, S., Temme, C., Ebinghaus, R., Steffen, A., Banic, C., Berg, T., Planchon, F., Barbant, C., Cescon, P., and Boutron, C. F.: Snow-to-air exchanges of mercury in an Arctic seasonal snow pack in Ny-Ålesund, Svalbard, Atmos. Environ., 39, 7633–7645, 2005. 22170

Fisher, J. A., Jacob, D. J., Soerensen, A. L., Amos, H. M., Steffen, A., and Sunderland, E. M.: Riverine source of Arctic Ocean mercury inferred from atmospheric observations, Nat. Geosci., 5, 499–504, doi:10.1038/NGEO1478, 2012. 22155, 22171

ACPD
13, 22151–22220, 2013

Fitzenberger, R., Bosch, H., Camy-Peyret, C., Chipperfield, M. P., Harder, H., Platt, U., Sinnhuber, B.-M., Wagner, T., and Pfeilsticker, K.: First profile measurements of tropospheric BrO, Geophys. Res. Lett., 27, 2921–2924, 2000. 22166

Fuller, E. N., Schettle, P. D., and Giddings, J. C.: A new method for prediction of binary gas-phase diffusion coefficients, Ind. Eng. Chem., 58, 19–27, 1966. 22160

Fuller, E. N., Ensley, K., and Giddings, J. C.: Diffusion of halogenated hydrocarbons in helium. Effect of structure on collision cross sections, J. Phys. Chem., 73, 3679–3685, 1969. 22160

Gårdfeldt, K. and Jonsson, M.: Is bimolecular reduction of Hg(II) complexes possible in aqueous systems of environmental importance, J. Phys. Chem. A, 107, 4478–4482, 2003. 22164, 22206

Gårdfeldt, K., Sommar, J., Strömberg, D., and Feng, X.: Oxidation of atomic mercury by hydroxyl radicals and photoinduced decomposition of methylmercury in the aqueous phase, Atmos. Environ., 35, 3039–3047, 2001. 22206

Gauchard, P.-A., Aspmo, K., Temme, C., Steffen, A., Ferrari, C., Berg, T., Ström, J., Kaleschke, L., Dommergue, A., Bahlmann, E., Magand, O., Planchon, F., Ebinghaus, R., Banic, C., Nagorski, S., Baussand, P., and Boutron, C.: Study of the origin of atmospheric mercury depletion events recorded in Ny-Ålesund, Svalbard, spring 2003, Atmos. Environ., 39, 7620–7632, 2005. 22177

Giannelli, V., Thomas, D. N., Haas, C., Kattner, G., Kennedy, H., and Dieckmann, G. S.: Behaviour of dissolved organic matter and inorganic nutrients during experimental sea-ice formation, Ann. Glaciol., 33, 317–321, 2001. 22182

Gladich, I., Pfalzgraff, W., Maršálek, O., Jungwirth, P., Roselová, M., and Neshyba, S.: Arrhenius analysis of anisotropic surface self-diffusion on the prismatic facet of ice, Phys. Chem. Chem. Phys., 13, 19960–19969, 2011. 22161

Goodsite, M. E., Plane, J. M. C., and Skov, H.: A theoretical study of the oxidation of Hg^0 to $HgBr_2$ in the troposphere, Environ. Sci. Technol., 38, 1772–1776, 2004. 22156, 22168, 22175, 22176, 22177, 22206

Goodsite, M. E., Plane, J. M. C., and Skov, H.: Correction to A Theoretical Study of the Oxidation of Hg0 to HgBr2 in the Troposphere, Environ. Sci. Tech., 46, 5262–5262, doi:10.1021/es301201c, 2012. 22156, 22162, 22175, 22206

Harder, S. L., Warren, S. G., Charlson, R. J., and Covert, D. S.: Filtering of air through snow as a mechanism for aerosol deposition to the Antarctic ice sheet, J. Geophys. Res., 101, 18729–18743, doi:10.1029/96JD01174, 1996. 22161

ACPD
13, 22151–22220, 2013

Hedgecock, I. M., Trunfio, G. A., Pirrone, N., and Sprovieri, F.: Mercury chemistry in the MBL: Mediterranean case and sensitivity studies using the AMCOTS (Atmospheric Mercury Chemistry over the Sea) model, Atmos. Environ., 39, 7217–7230, 2005. 22162, 22169

Hepler, L. G. and Olofsson, G.: Mercury: Thermodynamic properties, chemical equilibria, and standard potentials, Chem. Rev., 75, 585–602, 1975. 22185, 22187, 22188, 22206

Hirdman, D., Aspmo, K., Burkhart, J. F., Eckhardt, S., Sodemann, H., and Stohl, A.: Transport of mercury in the Arctic atmosphere: Evidence for a spring-time net sink and summer-time source, Geophys. Res. Lett., 36, L12814, doi:10.1029/2009GL038345, 2009. 22155, 22170

Holmes, C. D., Jacob, D. J., Mason, R. P., and Jaffe, D. A.: Sources and deposition of reactive gaseous mercury in the marine atmosphere, Atmos. Environ., 43, 2278–2285, 2009. 22185

Holmes, C. D., Jacob, D. J., Corbitt, E. S., Mao, J., Yang, X., Talbot, R., and Slemr, F.: Global atmospheric model for mercury including oxidation by bromine atoms, Atmos. Chem. Phys., 10, 12037–12057, doi:10.5194/acp-10-12037-2010, 2010. 22154, 22155, 22157, 22162, 22163, 22174, 22179

Huthwelker, T., Ammann, M., and Peter, T.: The Uptake of Acidic Gases on Ice, Chem. Rev., 106, 1375–1444, 2006. 22160

Inoue, J., Liu, J., Pinto, J. O., and Curry, J. A.: Intercomparison of Arctic regional climate models: Modeling clouds and radiation for SHEBA in May 1998, J. Climate, 19, 4167–4178, 2006. 22173

Iverfeldt, Å. and Lindqvist, O.: Determination of distribution equilibia between water and air (in Swedish with English summary), Report no. 415, Project Coal, Health and Environment, The Swedish State Power Board, S-16287, Vällingby, Sweden, 1980. 22163, 22206

Johnson, K. P., Blum, J. D., Keeler, G. J., and Douglas, T. A.: Investigation of the deposition and emission of mercury in arctic snow during an atmospheric mercury depletion event, J. Geophys. Res., 113, D17304, doi:10.1029/2008JD009893, 2008. 22154, 22164, 22170, 22216

Jones, A. E., Anderson, P. S., Begoin, M., Brough, N., Hutterli, M. A., Marshall, G. J., Richter, A., Roscoe, H. K., and Wolff, E. W.: BrO, blizzards, and drivers of polar tropospheric ozone depletion events, Atmos. Chem. Phys., 9, 4639–4652, doi:10.5194/acp-9-4639-2009, 2009. 22182

Khalizov, A. F., Viswanathan, B., Larregaray, P., and Ariya, P. A.: A theoretical study on the reactions of Hg with halogens: atmospheric implications, J. Phys. Chem. A, 107, 6360–6365., 2003. 22175

ACPD
13, 22151–22220, 2013

King, M. D. and Simpson, W. R.: Extinction of UV radiation in Arctic snow at Alert, Canada (82°N), J. Geophys. Res., 106, 12499–12507, 2001. 22161

Kirk, J. L., St. Louis, V. L., and Sharp, M. J.: Rapid reduction and reemission of mercury deposited into snowpacks during atmospheric mercury depletion events at Churchill, Manitoba, Canada, Environ. Sci. Tech., 40, 7590–7596, 2006. 22154, 22164, 22170, 22216

Koop, T., Kapilashrami, A., Molina, L. T., and Molina, M. J.: Phase transitions of sea-salt/water mixtures at low temperatures: Implications for ozone chemistry in the polar marine boundary layer, J. Geophys. Res., 105, 26393–26402, 2000. 22165

Korhonen, H., Carslaw, K. S., Spracklen, D. V., Ridley, D. A., and Ström, J.: A global model study of processes controlling aerosol size distributions in the Arctic spring and summer, J. Geophys. Res., 113, D08211, doi:10.1029/2007JD009114, 2008. 22173

Kylling, A., Stamnes, K., and Tsay, S.-C.: A reliable and efficient two-stream algorithm for spherical radiative transfer: Documentation of accuracy in realistic layered media, J. Atmos. Chem., 21, 115–150, 1995. 22161

Lalonde, J. D., Amyot, M., and Poulain, A. J.: The Role of Mercury Redox Reactions in Snow on Snow-to-Air Mercury Transfer, Environ. Sci. Technol., 36, 174–178, 2002. 22154

Lalonde, J. D., Amyot, M., Doyon, M.-R., and Auclair, J.-C.: Photo-induced Hg(II) reduction in snow from the remote and temperate Experimental Lakes Area (Ontario, Canada), J. Geophys. Res., 108, 4200, doi:10.1029/2001JD001534, 2003. 22154, 22163, 22164

Li, S.-M.: Equilibrium of particle nitrite with gas-phase HONO: tropospheric measurements in the high arctic during polar sunrise, J. Geophys. Res., 99, 25469–25478, 1994. 22185

Liao, J., Sihler, H., Huey, L. G., Neuman, J. A., Tanner, D. J., Friess, U., Platt, U., Flocke, F. M., Orlando, J. J., Shepson, P. B., Beine, H. J., Weinheimer, A. J., Sjostedt, S. J., Nowak, J. B., Knapp, D. J., Staebler, R. M., Zheng, W., Sander, R., Hall, S. R., and Ullmann, K.: A comparison of Arctic BrO measurements by chemical ionization mass spectrometry and long path differential optical absorption spectroscopy, J. Geophys. Res., 116, D00R02, doi:10.1029/2010JD014788, 2011. 22167

Lin, C.-J. and Pehkonen, S. O.: Oxidation of elemental mercury by aqueous chlorine ($HOCl/OCl^-$): Implications for tropospheric mercury chemistry, J. Geophys. Res., 103D, 28093–28102, 1998. 22206

Lindberg, S. E., Brooks, S., abd Karen J. Scott, C.-J. L., Landis, M. S., Stevens, R. K., Goodsite, M., and Richter, A.: Dynamic oxidation of gaseous mercury in the Arctic troposphere at polar sunrise, Environ. Sci. Technol., 36, 1245–1256, 2002. 22154, 22186

ACPD
13, 22151–22220, 2013

Lindqvist, O. and Rodhe, H.: Atmospheric mercury – a review, Tellus, 37B, 136–159, 1985. 22163, 22182
Lu, J. Y., Schroeder, W. H., Barrie, L. A., Steffen, A., Welch, H. E., Martin, K., Lockhart, L., Hunt, R. V., Boila, G., and Richter, A.: Magnification of atmospheric mercury deposition to polar regions in springtime: the link to tropospheric ozone depletion chemistry, Geophys. Res. Lett., 28, 3219–3222, 2001. 22154
Lyman, S. N., Jaffe, D. A., and Gustin, M. S.: Release of mercury halides from KCl denuders in the presence of ozone, Atmos. Chem. Phys., 10, 8197–8204, doi:10.5194/acp-10-8197-2010, 2010. 22171
Mantoura, R. F. C., Dickson, A., and Riley, J. P.: The complexation of metals with humic materials in natural waters, Estuar. Coastal Mar. Sci., 6, 387–408, 1978. 22182
Mao, H., Talbot, R. W., Sive, B. C., Kim, S. Y., Blake, D. R., and Weinheimer, A. J.: Arctic mercury depletion and its quantitative link with halogens, J. Atmos. Chem., 65, 145–170, 2010. 22166
Marcus, Y. and Eliezer, I.: Mercury(II) halide mixed complexes in solution. V. Comparison of calculated and experimental stability constants, J. Phys. Chem., 66, 1661–1663, 1962. 22187, 22188, 22189, 22206
Massman, W.: Molecular diffusivities of Hg vapor in air, O_2 and N_2 near STP and the kinematic viscosity and thermal diffusivity of air near STP, Atmos. Environ., 33, 453–457, 1999. 22160
Millero, F. J., Feistel, R., Wright, D. G., and McDougall, T. J.: The composition of Standard Seawater and the definition of the Reference-Composition Salinity Scale, Deep-Sea Res. Pt. I, 55, 50–72, 2008. 22182
Morin, S., Marion, G. M., von Glasow, R., Voisin, D., Bouchez, J., and Savarino, J.: Precipitation of salts in freezing seawater and ozone depletion events: a status report, Atmos. Chem. Phys., 8, 7317–7324, doi:10.5194/acp-8-7317-2008, 2008. 22165
Mulvaney, R., Wolff, E. W., and Oates, K.: Sulphuric acid at grain boundaries in Antarctic ice, Natrue, 331, 247–249, 1988. 22159
Munthe, J. and McElroy, W. J.: Some aqueous reactions of potential importance in the atmospheric chemistry of mercury, Atmos. Environ., 26A, 553–557, 1992. 22206
Nasello, O. B., Navarro de Juarez, S., and Di Prinzio, C. L.: Measurement of self-diffusion on ice surface, Scr. Mater., 56, 1071–1073, 2007. 22161
Nazhat, N. B. and Asmus, K.-D.: Reduction of mercuric chloride by hydrated electrons and reducing radicals in aqueous solutions. Formation and reactions of HgCl, J. Phys. Chem., 77, 614–620, 1973. 22164, 22206

ACPD
13, 22151–22220, 2013

Oltmans, S. J., Schnell, R. C., Sheridan, P. J., Peterson, R. E., Li, S.-M., Winchester, J. W., Tans, P. P., Sturges, W. T., Kahl, J. D., and Barrie, L. A.: Seasonal surface ozone and filterable bromine relationship in the high Arctic, Atmos. Environ., 23, 2431–2441, 1989. 22167

Outridge, P. M., Macdonald, R. W., Wang, F., Stern, G. A., and Dastoor, A. P.: A mass balance inventory of mercury in the Arctic Ocean, Environ. Chem., 5, 89–111, doi:10.1071/EN08002, 2008. 22155, 22171

Pal, B. and Ariya, P. A.: Studies of ozone initiated reactions of gaseous mercury: kinetics, product studies, and atmospheric implications, Phys. Chem. Chem. Phys., 6, 572–579, 2004. 22162

Parrella, J. P., Jacob, D. J., Liang, Q., Zhang, Y., Mickley, L. J., Miller, B., Evans, M. J., Yang, X., Pyle, J. A., Theys, N., and Roozendael, M. V.: Tropospheric bromine chemistry: implications for present and pre-industrial ozone and mercury, Atmos. Chem. Phys., 12, 6723–6740, doi:10.5194/acp-12-6723-2012, 2012. 22157, 22180

Pehkonen, S. O. and Lin, C. J.: Aqueous photochemistry of divalent mercury with organic acids, J. Air Waste Manage., 48, 144–150, 1998. 22164

Persson, P. O. G., Fairall, C. W., Andreas, E. L., Guest, P. S., and Perovich, D. K.: Measurements near the Atmospheric Surface Flux Group tower at SHEBA: Near-surface conditions and surface energy budget, J. Geophys. Res., 107, 8045, doi:10.1029/2000JC000705, 2002. 22160, 22164

Peterson, M. and Honrath, R.: Observations of rapid photochemical destruction of ozone in snowpack interstitial air, Geophys. Res. Lett., 28, 511–514, 2001. 22177

Peterson, M., Barber, D., and Green, S.: Monte Carlo modeling and measurements of actinic flux levels in Summit, Greenland snowpack, Atmos. Environ., 36, 2545–2551, 2002. 22161

Petroff, A. and Zhang, L.: Development and validation of a size-resolved particle dry deposition scheme for application in aerosol transport models, Geosci. Model Dev., 3, 753–769, doi:10.5194/gmd-3-753-2010, 2010. 22161

Platt, U. and Lehrer, E.: Arctic Tropospheric Ozone Chemistry, ARCTOC, Final Report of the EU-Project No. EV5V-CT93-0318, Heidelberg, 1996. 22154, 22167

Pleijel, K. and Munthe, J.: Modelling the atmospheric mercury cycle-chemistry in fog droplets, Atmos. Environ., 29, 1441–1457, 1995. 22206

Pöhler, D., Vogel, L., Frieß, U., and Platt, U.: Observation of halogen species in the Amundsen Gulf, Arctic, by active long-path differential optical absorption spectroscopy, P. Natl. Acad. Sci. USA, 107, 6582–6587, doi:10.1073/pnas.0912231107, 2010. 22165, 22167

ACPD
13, 22151–22220, 2013

Qiu, R., Green, S. A., Honrath, R. E., Peterson, M. C., Lu, Y., and Dziobak, M.: Measurements of $J_{NO_3^-}$ in snow by nitrate-based actinometry, Atmos. Environ., 36, 2563–2571, 2002. 22161
Quinn, P. K., Shaw, G., Andrews, E., Dutton, E. G., Ruoho-Airola, T., and Gong, S. L.: Arctic haze: current trends and knowledge gaps, Tellus, 59B, 99–114, 2007. 22164
Raofie, F. and Ariya, P. A.: Product study of the gas-phase BrO-initiated oxidation of Hg: evidence for stable Hg^{1+} compounds, Environ. Sci. Technol., 38, 4319–4326, 2004. 22156, 22162
Rosenthal, W., Saleta, J., and Dozier, J.: Scanning electron microscopy of impurity structures in snow, Cold Reg. Sci. Technol., 47, 80–89, 2007. 22159, 22160
Saiz-Lopez, A., Plane, J. M. C., Mahajan, A. S., Anderson, P. S., Bauguitte, S. J.-B., Jones, A. E., Roscoe, H. K., Salmon, R. A., Bloss, W. J., Lee, J. D., and Heard, D. E.: On the vertical distribution of boundary layer halogens over coastal Antarctica: implications for O_3, HO_x, NO_x and the Hg lifetime, Atmos. Chem. Phys., 8, 887–900, doi:10.5194/acp-8-887-2008, 2008. 22157, 22158, 22177
Sander, R., Vogt, R., Harris, G. W., and Crutzen, P. J.: Modeling the chemistry of ozone, halogen compounds, and hydrocarbons in the arctic troposphere during spring, Tellus, 49B, 522–532, 1997. 22167, 22184
Sander, R., Burrows, J., and Kaleschke, L.: Carbonate precipitation in brine – a potential trigger for tropospheric ozone depletion events, Atmos. Chem. Phys., 6, 4653–4658, doi:10.5194/acp-6-4653-2006, 2006. 22165
Sanemasa, I.: The solubility of elemental mercury vapor in water, Bull. Chem. Soc. Jpn., 48, 1795–1798, 1975. 22163, 22206
Schroeder, W. H., Anlauf, K. G., Barrie, L. A., Lu, J. Y., Steffen, A., R.Schneeberger, D., and Berg, T.: Arctic springtime depletion of mercury, Nature, 394, 331–332, 1998. 22154, 22168, 22179, 22216
Seigneur, C. and Lohman, K.: Effect of bromine chemistry on the atmospheric mercury cycle, J. Geophys. Res., 113, D23309, doi:10.1029/2008JD010262, 2008. 22163
Selin, N. E., Jacob, D. J., Park, R. J., Yantosca, R. M., Strode, S., Jaeglé, L., and Jaffe, D.: Chemical cycling and deposition of atmospheric mercury: Global constraints from observations, J. Geophys. Res., 112, D02308, doi:10.1029/2006JD007450, 2007. 22162
Shepler, B. C., Balabanov, N. B., and Peterson, K. A.: Hg + Br → HgBr recombination and collision-induced dissociation dynamics, J. Chem. Phys., 127, 164304, doi:10.1063/1.2777142, 2007. 22175, 22178

ACPD
13, 22151–22220, 2013

Shindell, D. T., Chin, M., Dentener, F., Doherty, R. M., Faluvegi, G., Fiore, A. M., Hess, P., Koch, D. M., MacKenzie, I. A., Sanderson, M. G., Schultz, M. G., Schulz, M., Stevenson, D. S., Teich, H., Textor, C., Wild, O., Bergmann, D. J., Bey, I., Bian, H., Cuvelier, C., Duncan, B. N., Folberth, G., Horowitz, L. W., Jonson, J., Kaminski, J. W., Marmer, E., Park, R., Pringle, K. J., Schroeder, S., Szopa, S., Takemura, T., Zeng, G., Keating, T. J., and Zuber, A.: A multi-model assessment of pollution transport to the Arctic, Atmos. Chem. Phys., 8, 5353–5372, doi:10.5194/acp-8-5353-2008, 2008. 22173

Si, L. and Ariya, P. A.: Reduction of oxidized mercury species by dicarboxylic acids (C2-C4): kinetic and product studies, Environ. Sci. Technol., 42, 5150–5155, 2008. 22163

Si, L. and Ariya, P. A.: Aqueous photoreduction of oxidized mercury species in presence of selected alkanethiols, Chemosphere, 84, 1079–1084, 2011. 22163

Sihler, H., Platt, U., Beirle, S., Marbach, T., Kühl, S., Dörner, S., Verschaeve, J., Frieß, U., Pöhler, D., Vogel, L., Sander, R., and Wagner, T.: Tropospheric BrO column densities in the Arctic derived from satellite: retrieval and comparison to ground-based measurements, Atmos. Meas. Tech., 5, 2779–2807, doi:10.5194/amt-5-2779-2012, 2012. 22180

Simpson, W. R., King, M. D., Beine, H. J., Honrath, R. E., and Zhou, X.: Radiation-transfer modeling of snow-pack photochemical processes during ALERT 2000, Atmos. Environ., 36, 2663–2670, 2002. 22161

Simpson, W. R., von Glasow, R., Riedel, K., Anderson, P., Ariya, P., Bottenheim, J., Burrows, J., Carpenter, L. J., Frieß, U., Goodsite, M. E., Heard, D., Hutterli, M., Jacobi, H.-W., Kaleschke, L., Neff, B., Plane, J., Platt, U., Richter, A., Roscoe, H., Sander, R., Shepson, P., Sodeau, J., Steffen, A., Wagner, T., and Wolff, E.: Halogens and their role in polar boundary-layer ozone depletion, Atmos. Chem. Phys., 7, 4375–4418, doi:10.5194/acp-7-4375-2007, 2007. 22153

Skov, H., Brooks, S. B., Goodsite, M. E., Lindberg, S. E., Meyers, T. P., Landis, M. S., Larsen, M. R., Jensen, B., McConville, G., and Christensen, J.: Fluxes of reactive gaseous mercury measured with a newly developed method using relaxed eddy accumulation, Atmos. Environ., 40, 5542–5463, 2006. 22157, 22172, 22186

Smith, R. S. and Kay, B. D.: The existence of supercooled liquid water at 150 K, Nature, 398, 788–791, 1999. 22161

Snider, G., Raofie, F., and Ariya, P. A.: Effects of relative humidity and CO(g) on the O_3-initiated oxidation reaction of Hg^0(g): kinetic and product studies, Phys. Chem. Chem. Phys., 10, 5616–5623, 2008. 22163

ACPD
13, 22151–22220, 2013

Sommar, J., Lindqvist, O., and Strömberg, D.: Distriution equilibrium of mercury (II) chloride between water and air applied to flue gas scrubbing, J. Air Waste Manage., 50, 1663–1666, 2000. 22163, 22206

Sommar, J., Andersson, M. E., and Jacobi, H.-W.: Circumpolar measurements of speciated mercury, ozone and carbon monoxide in the boundary layer of the Arctic Ocean, Atmos. Chem. Phys., 10, 5031–5045, doi:10.5194/acp-10-5031-2010, 2010. 22155

Spiro, T. G. and Hume, D. N.: A spectrophotometric study of the saturated mixed complexes of mercury(II)-bromide-iodide, Inorg. Chem., 2, 340–345, 1963. 22187, 22188

Staebler, R., Toom-Sauntry, D., Barrie, L., Langendörfer, U., Lehrer, E., Li, S.-M., and Dryfhout-Clark, H.: Physical and chemical characteristics of aerosols at Spitsbergen in the spring of 1996, J. Geophys. Res., 104D, 5515–5529, 1999. 22185, 22186

Steen, A. O., Berg, T., Dastoor, A. P., Durnford, D. A., Engelsen, O., Hole, L. R., and Pfaffhuber, K. A.: Natural and anthropogenic atmospheric mercury in the European Arctic: a fractionation study, Atmos. Chem. Phys., 11, 6273–6284, doi:10.5194/acp-11-6273-2011, 2011. 22157

Steeneveld, G. J., van de Wiel, B. J. H., and Holtslag, A. A. M.: Diagnostic equations for the stable boundary layer heights: Evaluation and dimensional analysis, J. Appl. Meteor. Clim., 46, 212–225, 2007. 22160

Steffen, A., Schroeder, W., Bottenheim, J., Narayan, J., and Fuentes, J. D.: Atmospheric mercury concentrations: measurements and profiles near snow and ice surfaces in the Canadian Arctic during Alert 2000, Atmos. Environ., 36, 2653–2661, 2002. 22154, 22170, 22176

Steffen, A., Douglas, T., Amyot, M., Ariya, P., Aspmo, K., Berg, T., Bottenheim, J., Brooks, S., Cobbett, F., Dastoor, A., Dommergue, A., Ebinghaus, R., Ferrari, C., Gardfeldt, K., Goodsite, M. E., Lean, D., Poulain, A. J., Scherz, C., Skov, H., Sommar, J., and Temme, C.: A synthesis of atmospheric mercury depletion event chemistry in the atmosphere and snow, Atmos. Chem. Phys., 8, 1445–1482, doi:10.5194/acp-8-1445-2008, 2008. 22153

Steffen, A., Bottenheim, J., Cole, A., Douglas, T. A., Ebinghaus, R., Friess, U., Netcheva, S., Nghiem, S., Sihler, H., and Staebler, R.: Atmospheric mercury over sea ice during the OASIS-2009 campaign, Atmos. Chem. Phys. Discuss., 13, 5687–5728, doi:10.5194/acpd-13-5687-2013, 2013a. 22170, 22185

Steffen, A., Bottenheim, J., Cole, A., Ebinghaus, R., Lawson, G., and Leaitch, W. R.: Understanding atmospheric mercury speciation and mercury in snow over time at Alert, Canada, Atmos. Chem. Phys. Discuss., 13, 17 021–17 052, doi:10.5194/acpd-13-17021-2013, 2013b. 22171, 22172, 22173, 22185, 22186

ACPD
13, 22151–22220, 2013

Stephens, C. R., Shepson, P. B., Steffen, A., Bottenheim, J. W., Liao, J., Huey, L. G., Apel, E., Weinheimer, A., Hall, S. R., Cantrell, C., Sive, B. C., Knapp, D. J., Montzka, D. D., and Hornbrook, R. S.: The relative importance of chlorine and bromine radicals in the oxidation of atmospheric mercury at Barrow, Alaska, J. Geophys. Res., 117, D00R11, doi:10.1029/2011JD016649, 2012. 22174

Subir, M., Ariya, P. A., and Dastoor, A. P.: A review of uncertainties in atmospheric modeling of mercury chemistry I. Uncertainties in existing kinetic parameters Fundamental limitations and the importance of heterogeneous chemistry, Atmos. Environ., 45, 5664–5676, 2011. 22155, 22162, 22174, 22175, 22178

Subir, M., Ariya, P. A., and Dastoor, A. P.: A review of the sources of uncertainties in atmospheric mercury modeling II. Mercury surface and heterogeneous chemistry A missing link, Atmos. Environ., 46, 1–10, 2012. 22157, 22163, 22178

Tarasick, D. W. and Bottenheim, J. W.: Surface ozone depletion episodes in the Arctic and Antarctic from historical ozonesonde records, Atmos. Chem. Phys., 2, 197–205, doi:10.5194/acp-2-197-2002, 2002. 22165, 22177

Theys, N., Van Roozendael, M., Hendrick, F., Yang, X., De Smedt, I., Richter, A., Begoin, M., Errera, Q., Johnston, P. V., Kreher, K., and De Mazière, M.: Global observations of tropospheric BrO columns using GOME-2 satellite data, Atmos. Chem. Phys., 11, 1791–1811, doi:10.5194/acp-11-1791-2011, 2011. 22180

Thomas, D. N., Kattner, G., Engbrodt, R., Giannelli, V., Kennedy, H., Haas, C., and Dieckmann, G. S.: Dissolved organic matter in Antarctic sea ice, Ann. Glaciol., 33, 297–303, 2001. 22183

Thomas, J. L., Stutz, J., Lefer, B., Huey, L. G., Toyota, K., Dibb, J. E., and von Glasow, R.: Modeling chemistry in and above snow at Summit, Greenland – Part 1: Model description and results, Atmos. Chem. Phys., 11, 4899–4914, doi:10.5194/acp-11-4899-2011, 2011. 22159

Toyota, K., Takahashi, M., and Akimoto, H.: Modeling multi-phase halogen chemistry in the marine boundary layer with size-segregated aerosol module: Implications for quasi-size-dependent approach, Geophys. Res. Lett., 28, 2899–2902, 2001. 22159

Toyota, K., Kanaya, Y., Takahashi, M., and Akimoto, H.: A box model study on photochemical interactions between VOCs and reactive halogen species in the marine boundary layer, Atmos. Chem. Phys., 4, 1961–1987, doi:10.5194/acp-4-1961-2004, 2004. 22159

Toyota, K., McConnell, J. C., Lupu, A., Neary, L., McLinden, C. A., Richter, A., Kwok, R., Semeniuk, K., Kaminski, J. W., Gong, S.-L., Jarosz, J., Chipperfield, M. P., and Sioris, C. E.: Analysis of reactive bromine production and ozone depletion in the Arctic boundary layer

ACPD
13, 22151–22220, 2013

using 3-D simulations with GEM-AQ: inference from synoptic-scale patterns, Atmos. Chem. Phys., 11, 3949–3979, doi:10.5194/acp-11-3949-2011, 2011. 22180
Toyota, K., McConnell, J. C., Staebler, R. M., and Dastoor, A. P.: Air-snowpack exchange of bromine, ozone and mercury in the springtime Arctic simulated by the 1-D model PHANTAS – Part 1: In-snow bromine activation and its impact on ozone, Atmos. Chem. Phys. Discuss., 13, 20 341–20 418, doi:10.5194/acpd-13-20341-2013, 2013. 22158, 22161, 22164, 22165, 22166, 22167, 22169, 22175, 22179, 22182, 22183, 22184
Tuckermann, M., Ackermann, R., Göltz, C., Lorenzen-schmidt, H., Senne, T., Stutz, J., Trost, B., Unold, W., and Platt, U.: DOAS-observation of halogen radical-catalysed arctic boundary layer ozone destruction during the ARCTOC-campaigns 1995 and 1996 in Ny-Ålesund, Spitsbergen, Tellus, 49B, 533–555, 1997. 22167
Van Loon, L., Mader, E., and Scott, S. L.: Reduction of the Aqueous Mercuric Ion by Sulfite: UV Spectrum of $HgSO_3$ and Its Intramolecular Redox Reaction, J. Phys. Chem. A, 104, 1621–1626, 2000. 22164
Van Loon, L., Mader, E., and Scott, S. L.: Sulfite Stabilization and Reduction of the Aqueous Mercuric Ion: Kinetic Determination of Sequential Formation Constants, J. Phys. Chem. A, 105, 3190–3195, 2001. 22164
Wagman, D., Evans, W., Parker, V., Schumm, R., Halow, I., Bailey, S., Churney, K., and Nuttall, R.: The NBS Tables of Chemical of Chemical Thermodynamic Properties, J. Phys. Chem. Ref. Data, 11 (Suppl. 2), 1982. 22185, 22187, 22188, 22206
Wang, Z. and Pehkonen, S. O.: Oxidation of elemental mercury by aqueous bromine: atmospheric implications, Atmos. Environ., 38, 3675–3688, 2004. 22206
Warren, S. G. and Wiscombe, W. J.: A model for the spectral albedo of snow. II: Snow containing atmospheric aerosols, J. Atmos. Sci., 37, 2734–2745, 1980. 22161
Warren, S. G., Rigor, I. G., Untersteiner, N., Radionov, V. F., Bryazgin, N. N., Aleksandrov, Y. I., and Colony, R.: Snow depth on Arctic sea ice, J. Climate, 12, 1814–1829, 1999. 22159
Wennberg, P.: Bromine explosion, Nature, 397, 299–301, 1999. 22154, 22167
Wolff, E. W. and Paren, J. G.: A two-phase model of electrical conduction in polar ice sheets, J. Geophys. Res., 89B, 9433–9438, 1984. 22160
Xiao, Z. F., Strömberg, D., and Lindqvist, O.: Influence of humic substances on photolysis of divalent mercury in aqueous solution, Water Air Soil Pollut., 80, 789–798, 1995. 22163
Xie, Z.-Q., Sander, R., Pöschl, U., and Slemr, F.: Simulation of atmospheric mercury depletion events (AMDEs) during polar springtime using the MECCA box model, Atmos. Chem. Phys.,

ACPD
13, 22151–22220, 2013

8, 7165–7180, doi:10.5194/acp-8-7165-2008, 2008. 22157, 22158, 22162, 22163, 22166, 22169, 22174

Yang, X., Pyle, J. A., and Cox, R. A.: Sea salt aerosol production and bromine release: Role of snow on sea ice, Geophys. Res. Lett., 35, L16815, doi:10.1029/2008GL034536, 2008. 22159, 22182, 22186

Zeng, T., Wang, Y., Chance, K., Blake, N., Blake, D., and Ridley, B.: Halogen-driven low-altitude O_3 and hydrocarbon losses in spring at northern high latitudes, J. Geophys. Res., 111, D17313, doi:10.1029/2005JD006706, 2006. 22180

ACPD

13, 22151–22220, 2013

Table 1. List of reactions and multiphase mass transfers for mercury species included in the model.

Gas-phase reactions			
Reaction	Rate constant	Unit	Reference
$Hg + Br + M \rightarrow HgBr + M$	$k = 1.44 \times 10^{-32}(T/300)^{-1.86}$[M]	[cm^3 $molecule^{-1}$ s^{-1}]	1
$HgBr + M \rightarrow Hg + Br + M$	$k = 4.0 \times 10^{9} \exp(-7292/T)$	[s^{-1}]	2
$HgBr + Br \rightarrow HgBr_2$	$k = 2.5 \times 10^{-12}(T/300)^{-0.57}$	[cm^3 $molecule^{-1}$ s^{-1}]	3
$HgBr + Br \rightarrow Hg + Br_2$	$k = 3.9 \times 10^{-11}$	[cm^3 $molecule^{-1}$ s^{-1}]	4
$HgBr + BrO \rightarrow Hg(OBr)Br$	$k = 2.5 \times 10^{-12}(T/300)^{-0.57}$	[cm^3 $molecule^{-1}$ s^{-1}]	($= k_{HgBr+Br}$)
$Hg(OBr)Br + h\nu \rightarrow Hg(O)Br + Br$	J_{HOBr}	[s^{-1}]	5
$Hg(O)Br + HO_2 \rightarrow Hg(OH)Br + O_2$	$k = 2.2 \times 10^{-11}$	[cm^3 $molecule^{-1}$ s^{-1}]	5
Henry's law equilibria, equilibrium constants given by $K_H = K_H^{\ominus} \exp[-\Delta H_{solv}^{\ominus}/R \times (1/T - 1/T^{\ominus})]$			
Reaction	$K_H^{\ominus}$	Unit	$-\Delta H_{solv}^{\ominus}/R$	Unit	Reference
$Hg(gas) \rightleftarrows Hg(aq)$	1.28×10^{-1}	[M atm^{-1}]	2482	[K]	6
$Hg(OH)_2(gas) \rightleftarrows Hg(OH)_2(aq)$	1.28×10^{4}	[M atm^{-1}]	3901	[K]	7
$HgCl_2(gas) \rightleftarrows HgCl_2(aq)$	1.00×10^{6}	[M atm^{-1}]	8060	[K]	8
$HgBr_2(gas) \rightleftarrows HgBr_2(aq)$	1.17×10^{5}	[M atm^{-1}]	8912	[K]	9
$Hg(OH)Cl(gas) \rightleftarrows Hg(OH)Cl(aq)$	1.00×10^{6}	[M atm^{-1}]	8060	[K]	($= K_{H,HgCl_2}$)
$HgClBr(gas) \rightleftarrows HgClBr(aq)$	1.00×10^{6}	[M atm^{-1}]	8060	[K]	($= K_{H,HgCl_2}$)
$Hg(OH)Br(gas) \rightleftarrows Hg(OH)Br(aq)$	1.17×10^{5}	[M atm^{-1}]	8912	[K]	($= K_{H,HgBr_2}$)
$Hg(OBr)Br(gas) \rightleftarrows Hg(OBr)Br(aq)$	1.17×10^{5}	[M atm^{-1}]	8912	[K]	($= K_{H,HgBr_2}$)
Aqueous-phase equilibria, equilibrium constants given by $K_{eq} = K_{eq}^{\ominus} \exp[-\Delta H_{rxn}^{\ominus}/R \times (1/T - 1/T^{\ominus})]$					
Reaction	$K_{eq}^{\ominus}$	Unit	$-\Delta H_{rxn}^{\ominus}/R$	Unit	Reference
$Hg^{2+} + OH^- \rightleftarrows HgOH^+$	2.62×10^{10}	[M^{-1}]	2966	[K]	9, 10
$HgOH^+ + OH^- \rightleftarrows Hg(OH)_2$	2.70×10^{11}	[M^{-1}]	5449	[K]	9, 10
$Hg^{2+} + Cl^- \rightleftarrows HgCl^+$	5.50×10^{6}	[M^{-1}]	2730	[K]	9, 10
$HgCl^+ + Cl^- \rightleftarrows HgCl_2$	2.55×10^{6}	[M^{-1}]	3637	[K]	9, 10
$HgCl_2 + Cl^- \rightleftarrows HgCl_3^-$	6.86×10^{0}	[M^{-1}]	630	[K]	9, 10
$HgCl_3^- + Cl^- \rightleftarrows HgCl_4^{2-}$	1.31×10^{1}	[M^{-1}]	−223	[K]	9, 10
$Hg^{2+} + Br^- \rightleftarrows HgBr^+$	1.07×10^{9}	[M^{-1}]	5196	[K]	9, 10
$HgBr^+ + Br^- \rightleftarrows HgBr_2$	2.50×10^{8}	[M^{-1}]	5454	[K]	9, 10
$HgBr_2 + Br^- \rightleftarrows HgBr_3^-$	1.45×10^{2}	[M^{-1}]	1329	[K]	9, 10
$HgBr_3^- + Br^- \rightleftarrows HgBr_4^{2-}$	2.27×10^{1}	[M^{-1}]	1942	[K]	9, 10
$HgOH^+ + Cl^- \rightleftarrows Hg(OH)Cl$	6.70×10^{6}	[M^{-1}]	4455	[K]	9, 10
$HgOH^+ + Br^- \rightleftarrows Hg(OH)Br$	1.25×10^{9}	[M^{-1}]	4455	[K]	9, 10, see Note[a]
$HgCl^+ + OH^- \rightleftarrows Hg(OH)Cl$	3.19×10^{10}	[M^{-1}]	4691	[K]	9, 10
$HgBr^+ + OH^- \rightleftarrows Hg(OH)Br$	3.06×10^{10}	[M^{-1}]	4691	[K]	9, 10, see Note[a]
$HgCl_2 + Br^- \rightleftarrows HgClBr + Cl^-$	3.37×10^{2}	non-dimensional	2200	[K]	9, 10, 11
$HgClBr + Br^- \rightleftarrows HgBr_2 + Cl^-$	5.67×10^{1}	non-dimensional	2083	[K]	9, 10, 11
$HgCl_3^- + Br^- \rightleftarrows HgCl_2Br^- + Cl^-$	3.05×10^{2}	non-dimensional	1755	[K]	9, 10, 11
$HgCl_2Br^- + Br^- \rightleftarrows HgClBr_2^- + Cl^-$	7.38×10^{1}	non-dimensional	1661	[K]	9, 10, 11
$HgClBr_2^- + Br^- \rightleftarrows HgBr_3^- + Cl^-$	1.80×10^{1}	non-dimensional	1566	[K]	9, 10, 11
$HgCl_4^{2-} + Br^- \rightleftarrows HgCl_3Br^{2-} + Cl^-$	1.87×10^{2}	non-dimensional	1929	[K]	9, 10, 11
$HgCl_3Br^{2-} + Br^- \rightleftarrows HgCl_2Br_2^{2-} + Cl^-$	5.07×10^{1}	non-dimensional	1834	[K]	9, 10, 11
$HgCl_2Br_2^{2-} + Br^- \rightleftarrows HgClBr_3^{2-} + Cl^-$	1.64×10^{1}	non-dimensional	1740	[K]	9, 10, 11
$HgClBr_3^{2-} + Br^- \rightleftarrows HgBr_4^{2-} + Cl^-$	4.50×10^{0}	non-dimensional	1645	[K]	9, 10, 11

ACPD
13, 22151–22220, 2013

Table 1. Continued.

Aqueous-phase reactions			
Reaction	Rate constant	Unit	Reference
$Hg + O_3 \rightarrow HgO + O_2$	$k = 4.7 \times 10^7$	$[M^{-1}\,s^{-1}]$	12
$HgO + H^+ \rightarrow Hg^{2+} + OH^-$	$k = 1.0 \times 10^{10}$	$[M^{-1}\,s^{-1}]$	13
$Hg + OH \rightarrow Hg^+ + OH^-$	$k = 2.4 \times 10^9$	$[M^{-1}\,s^{-1}]$	14
$Hg^+ + O_2 \rightarrow Hg^{2+} + O_2^-$	$k = 1.0 \times 10^9$	$[M^{-1}\,s^{-1}]$	15
$Hg^+ + OH \rightarrow Hg^{2+} + OH^-$	$k = 1.0 \times 10^{10}$	$[M^{-1}\,s^{-1}]$	15
$Hg + HOCl \rightarrow Hg^{2+} + Cl^- + OH^-$	$k = 2.09 \times 10^6$	$[M^{-1}\,s^{-1}]$	16
$Hg + ClO^- \rightarrow Hg^{2+} + Cl^- + 2\,OH^-$	$k = 1.99 \times 10^8$	$[M^{-1}\,s^{-1}]$	16
$Hg + HOBr \rightarrow Hg^{2+} + Br^- + OH^-$	$k = 2.79 \times 10^{-1}$	$[M^{-1}\,s^{-1}]$	17
$Hg + BrO^- \rightarrow Hg^{2+} + Br^- + 2\,OH^-$	$k = 2.73 \times 10^{-1}$	$[M^{-1}\,s^{-1}]$	17
$Hg + Br_2 \rightarrow Hg^{2+} + 2\,Br^-$	$k = 1.96 \times 10^{-1}$	$[M^{-1}\,s^{-1}]$	17
$Hg^{2+} + O_2^- \rightarrow Hg^+ + O_2$	$k = 5.0 \times 10^3$	$[M^{-1}\,s^{-1}]$	18
$Hg^{2+} + HO_2 \rightarrow Hg^+ + O_2 + H+$	$k = 5.0 \times 10^3$	$[M^{-1}\,s^{-1}]$	$(= k_{Hg^{2+}+O_2^-})$
$Hg^+ + O_2^- \rightarrow Hg + O_2$	$k = 1.0 \times 10^{10}$	$[M^{-1}\,s^{-1}]$	see Note[b]
$Hg^+ + HO_2 \rightarrow Hg + O_2 + H+$	$k = 1.0 \times 10^{10}$	$[M^{-1}\,s^{-1}]$	see Note[b]
$Hg(OBr)Br + h\nu \rightarrow Hg(O)Br + Br$	J_{HOBr}	$[s^{-1}]$	see Note[c]
$Hg(O)Br + HO_2 \rightarrow Hg(OH)Br + O_2$	$k = 1.0 \times 10^{10}$	$[M^{-1}\,s^{-1}]$	see Note[c]
$Hg(O)Br + O_2^- \rightarrow Hg(OH)Br + O_2 + OH^-$	$k = 1.0 \times 10^{10}$	$[M^{-1}\,s^{-1}]$	see Note[c]
$Hg^{2+} + h\nu \xrightarrow{2e^-} Hg$	$\alpha \times J_{O_3 \rightarrow O(^1D)}$	$[s^{-1}]$	see Note[d]
$HgOH^+ + h\nu \xrightarrow{2e^-} Hg + OH^-$	$\alpha \times J_{O_3 \rightarrow O(^1D)}$	$[s^{-1}]$	see Note[d]
$Hg(OH)_2 + h\nu \xrightarrow{2e^-} Hg + 2\,OH^-$	$\alpha \times J_{O_3 \rightarrow O(^1D)}$	$[s^{-1}]$	see Note[d]
$HgCl^+ + h\nu \xrightarrow{2e^-} Hg + Cl^-$	$\alpha \times J_{O_3 \rightarrow O(^1D)}$	$[s^{-1}]$	see Note[d]
$HgCl_2 + h\nu \xrightarrow{2e^-} Hg + 2\,Cl^-$	$\alpha \times J_{O_3 \rightarrow O(^1D)}$	$[s^{-1}]$	see Note[d]
$HgCl_3^- + h\nu \xrightarrow{2e^-} Hg + 3\,Cl^-$	$\alpha \times J_{O_3 \rightarrow O(^1D)}$	$[s^{-1}]$	see Note[d]
$HgCl_4^{2-} + h\nu \xrightarrow{2e^-} Hg + 4\,Cl^-$	$\alpha \times J_{O_3 \rightarrow O(^1D)}$	$[s^{-1}]$	see Note[d]
$HgBr_+ + h\nu \xrightarrow{2e^-} Hg + Br^-$	$\alpha \times J_{O_3 \rightarrow O(^1D)}$	$[s^{-1}]$	see Note[d]
$HgBr_2 + h\nu \xrightarrow{2e^-} Hg + 2\,Br^-$	$\alpha \times J_{O_3 \rightarrow O(^1D)}$	$[s^{-1}]$	see Note[d]
$HgBr_3^- + h\nu \xrightarrow{2e^-} Hg + 3\,Br^-$	$\alpha \times J_{O_3 \rightarrow O(^1D)}$	$[s^{-1}]$	see Note[d]
$HgBr_4^{2-} + h\nu \xrightarrow{2e^-} Hg + 4\,Br^-$	$\alpha \times J_{O_3 \rightarrow O(^1D)}$	$[s^{-1}]$	see Note[d]
$Hg(OH)Cl + h\nu \xrightarrow{2e^-} Hg + OH^- + Cl^-$	$\alpha \times J_{O_3 \rightarrow O(^1D)}$	$[s^{-1}]$	see Note[d]
$Hg(OH)Br + h\nu \xrightarrow{2e^-} Hg + OH^- + Br^-$	$\alpha \times J_{O_3 \rightarrow O(^1D)}$	$[s^{-1}]$	see Note[d]
$HgClBr + h\nu \xrightarrow{2e^-} Hg + Cl^- + Br^-$	$\alpha \times J_{O_3 \rightarrow O(^1D)}$	$[s^{-1}]$	see Note[d]
$HgCl_2Br^- + h\nu \xrightarrow{2e^-} Hg + 2\,Cl^- + Br^-$	$\alpha \times J_{O_3 \rightarrow O(^1D)}$	$[s^{-1}]$	see Note[d]
$HgClBr_2^- + h\nu \xrightarrow{2e^-} Hg + Cl^- + 2\,Br^-$	$\alpha \times J_{O_3 \rightarrow O(^1D)}$	$[s^{-1}]$	see Note[d]
$HgCl_3Br^{2-} + h\nu \xrightarrow{2e^-} Hg + 3\,Cl^- + Br^-$	$\alpha \times J_{O_3 \rightarrow O(^1D)}$	$[s^{-1}]$	see Note[d]
$HgCl_2Br_2^{2-} + h\nu \xrightarrow{2e^-} Hg + 2\,Cl^- + 2\,Br^-$	$\alpha \times J_{O_3 \rightarrow O(^1D)}$	$[s^{-1}]$	see Note[d]
$HgClBr_3^{2-} + h\nu \xrightarrow{2e^-} Hg + Cl^- + 3\,Br^-$	$\alpha \times J_{O_3 \rightarrow O(^1D)}$	$[s^{-1}]$	see Note[d]

References: 1. Donohoue et al. (2006); 2. Goodsite et al. (2012); 3. Goodsite et al. (2004); 4. Balabanov et al. (2005); 5. Calvert and Lindberg (2004); 6. Sanemasa (1975); 7. Iverfeldt and Lindqvist (1980); 8. Sommar et al. (2000); 9. Hepler and Olofsson (1975); 10. Wagman et al. (1982); 11. Marcus and Eliezer (1962); 12. Munthe and McElroy (1992); 13. Pleijel and Munthe (1995); 14. Gårdfeldt et al. (2001); 15. Nazhat and Asmus (1973); 16. Lin and Pehkonen (1998); 17. Wang and Pehkonen (2004); 18. Gårdfeldt and Jonsson (2003).

[a] Temperature dependence is taken from K_H for ClHgOH; [b] Assumed to be very fast; [c] Analogically expanded from gas-phase reactions; [d] See Sect. 2.2.

ACPD
13, 22151–22220, 2013

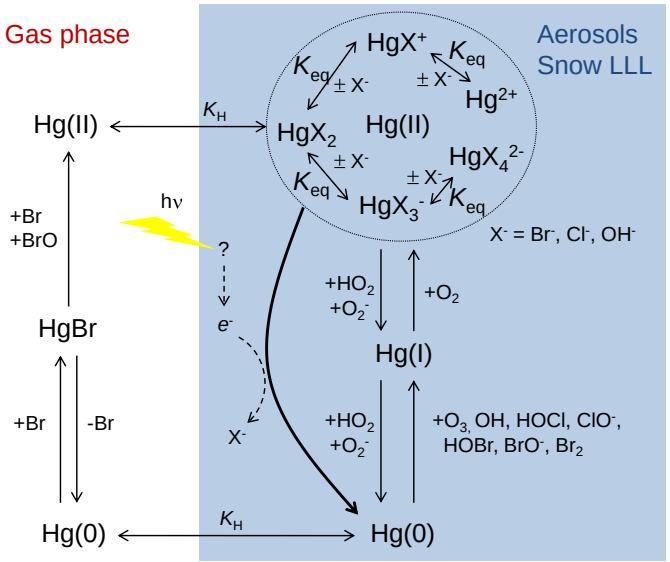

Fig. 1. Outline of mercury chemical mechanism in PHANTAS.

ACPD
13, 22151–22220, 2013

Photochemistry of mercury and its speciation during AMDEs

K. Toyota et al.

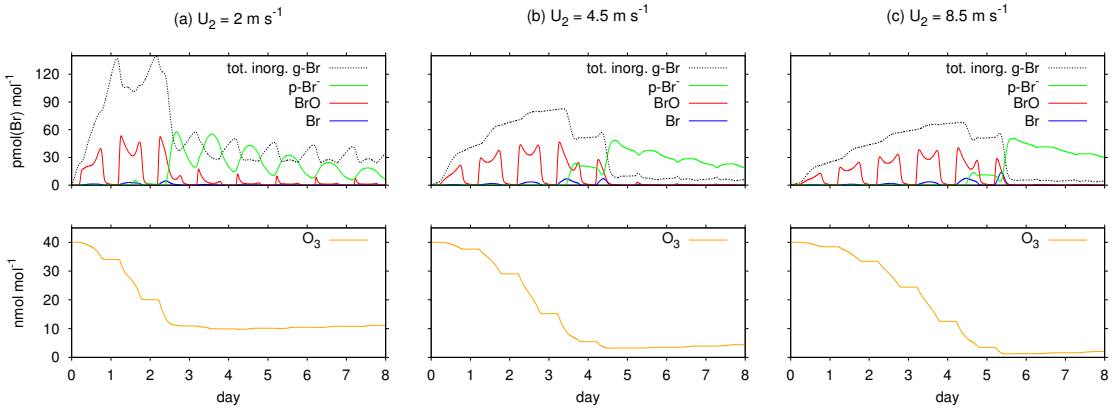

Fig. 2. Temporal evolution for the mixing ratios of inorganic bromine species (top row) and ozone (bottom row) at the height of 1.5 m in the ambient air from model runs at U_2 = 2.0 m s^{-1} **(a)**, 4.5 m s^{-1} **(b)**, and 8.5 m s^{-1} **(c)**. Total inorganic gaseous bromine in dotted black lines, particulate (or aerosol) bromide in green lines, BrO radical in red lines, Br-atom in blue lines and ozone in orange lines.

ACPD
13, 22151–22220, 2013

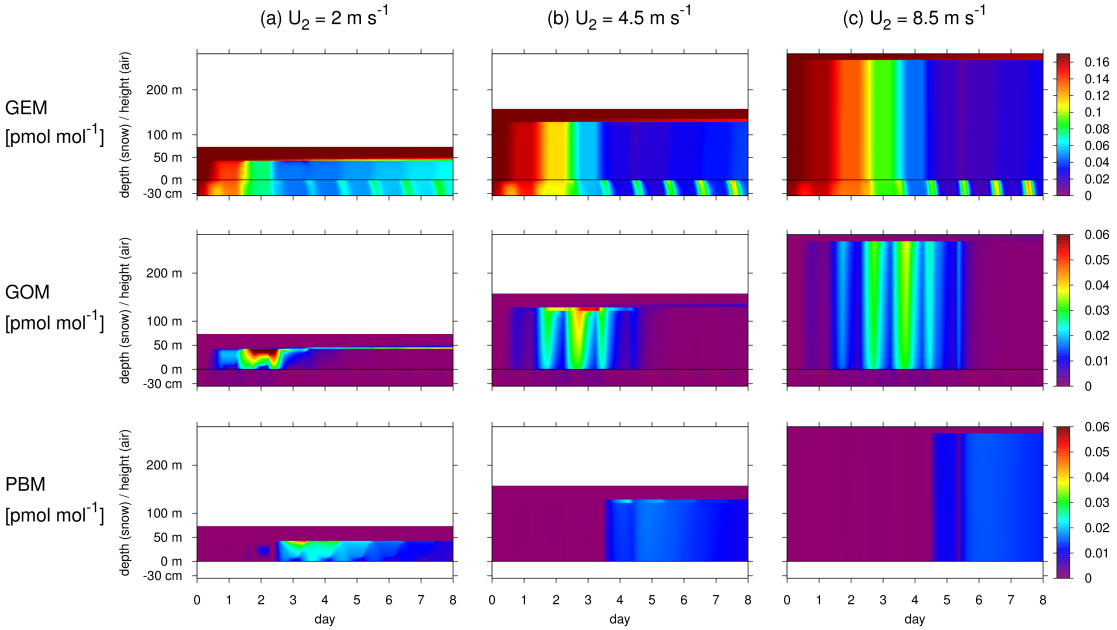

Fig. 3. Time-height cross sections for the mixing ratios of GEM (top row), GOM (middle row), and PBM (bottom row) from model runs at U_2 = 2.0 m s^{-1} **(a)**, 4.5 m s^{-1} **(b)**, and 8.5 m s^{-1} **(c)**.

ACPD
13, 22151–22220, 2013

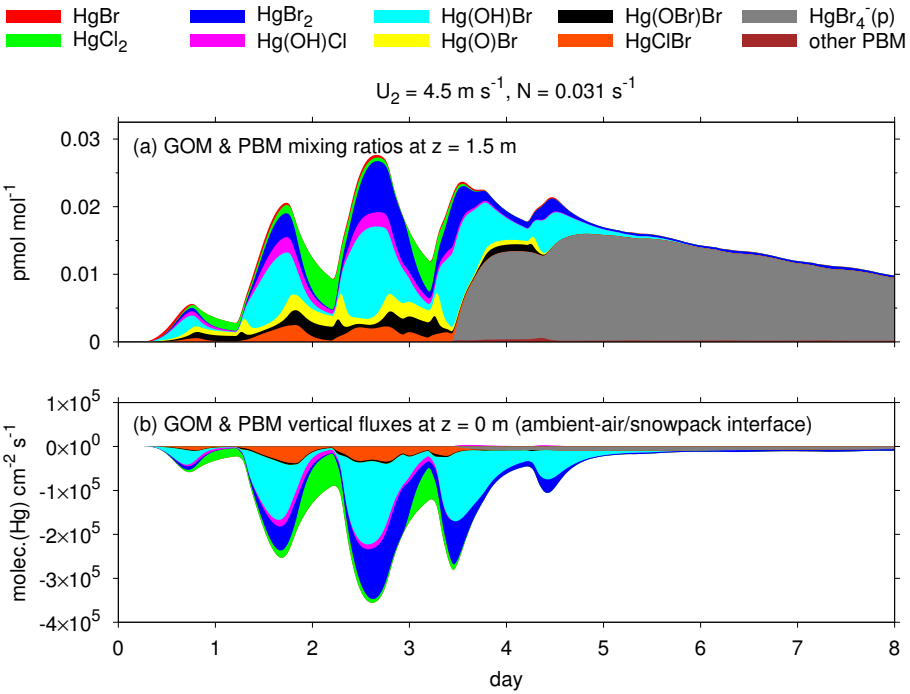

Fig. 4. Speciation and vertical fluxes of GOM and PBM as simulated at $U_2 = 4.5\,\mathrm{m\,s^{-1}}$: **(a)** mixing ratios of GOM and PBM species at $z = 1.5\,\mathrm{m}$ in ambient air above the snowpack and **(b)** vertical fluxes of GOM and PBM species at $z = 0\,\mathrm{m}$, i.e. between ambient air and snowpack. Because of very low mixing ratios simulated, gaseous $Hg(OH)_2$ is neglected in these plots.

ACPD
13, 22151–22220, 2013

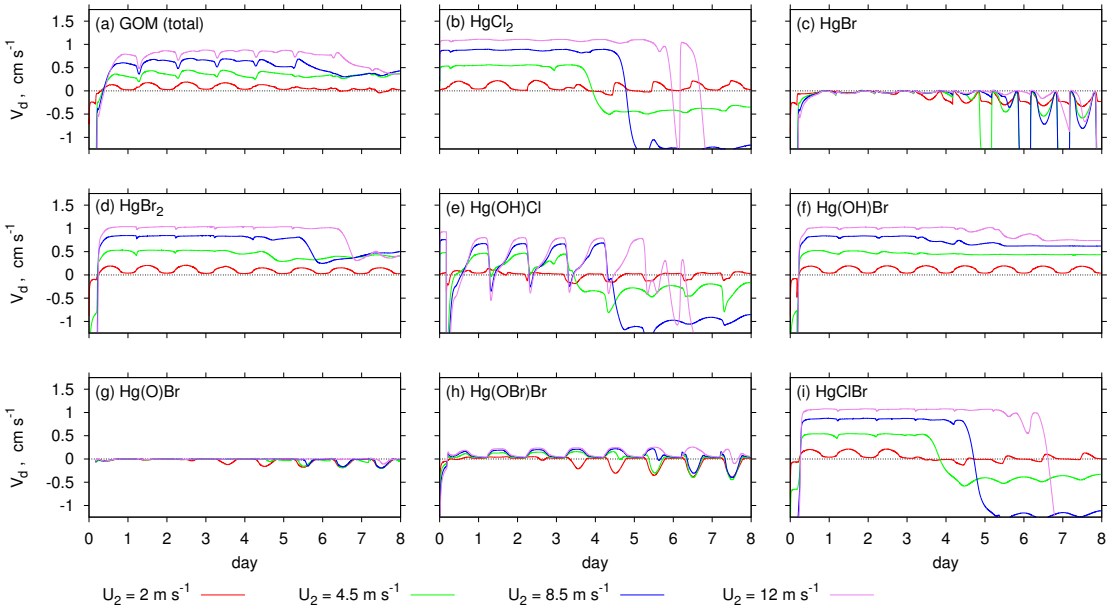

Fig. 5. Apparent dry deposition velocities of GOM and its each component species (except $Hg(OH)_2$, which constitutes a minimal partitioning in GOM simulated here) at 1.5 m above the snow surface from model runs at $U_2 = 2.0\,m\,s^{-1}$ (red lines), $4.5\,m\,s^{-1}$ (green lines), $8.5\,m\,s^{-1}$ (blue lines), and $12.0\,m\,s^{-1}$ (violet lines): **(a)** the sum of all GOM species, **(b)** $HgCl_2$, **(c)** HgBr, **(d)** $HgBr_2$, **(e)** Hg(OH)Cl, **(f)** Hg(OH)Br, **(g)** Hg(O)Br, **(h)** Hg(OBr)Br, and **(i)** HgClBr.

ACPD
13, 22151–22220, 2013

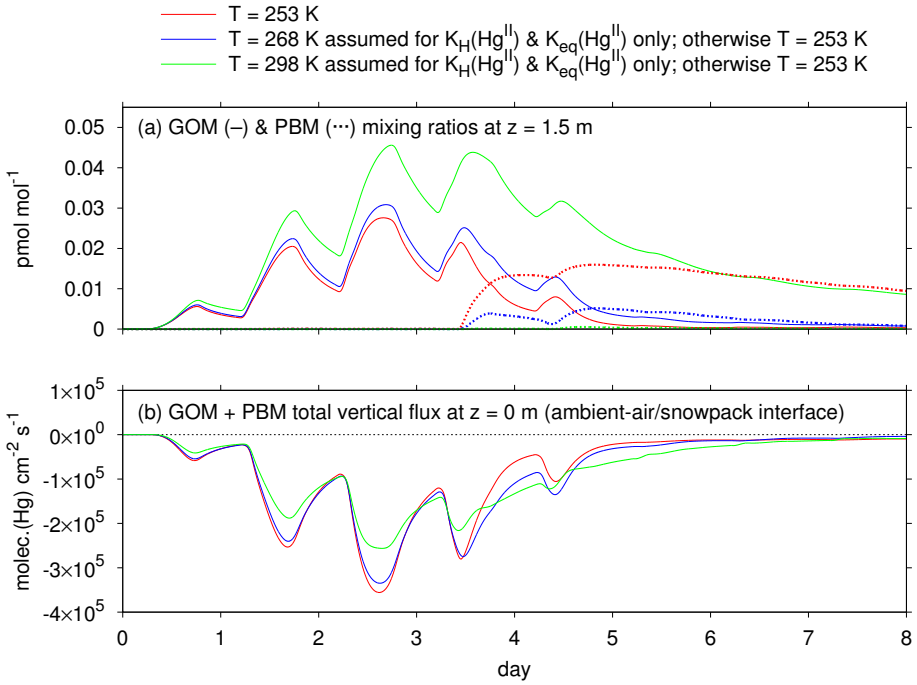

Fig. 6. Sensitivities of partitioning between GOM and PBM in the ambient air and their total air-snow fluxes on the choice of temperature-dependent thermodynamic parameters for Hg(II) species: **(a)** mixing ratios of GOM (solid lines) and PBM (dotted lines) simulated at z = 1.5 m in the ambient air above the snowpack and **(b)** total vertical fluxes of GOM and PBM at z = 0 m. Red lines denote a base case from a model run at U_2 = 4.5 m s^{-1} and T = 253 K. Blue and green lines denote sensitivity runs performed with the same condition except that, for the calculations of Henry's law (K_H) and aqueous-phase stability constants for halide complexes (K_{eq}) of Hg(II) species, T = 268 K and 298 K, respectively, were assumed.

ACPD
13, 22151–22220, 2013

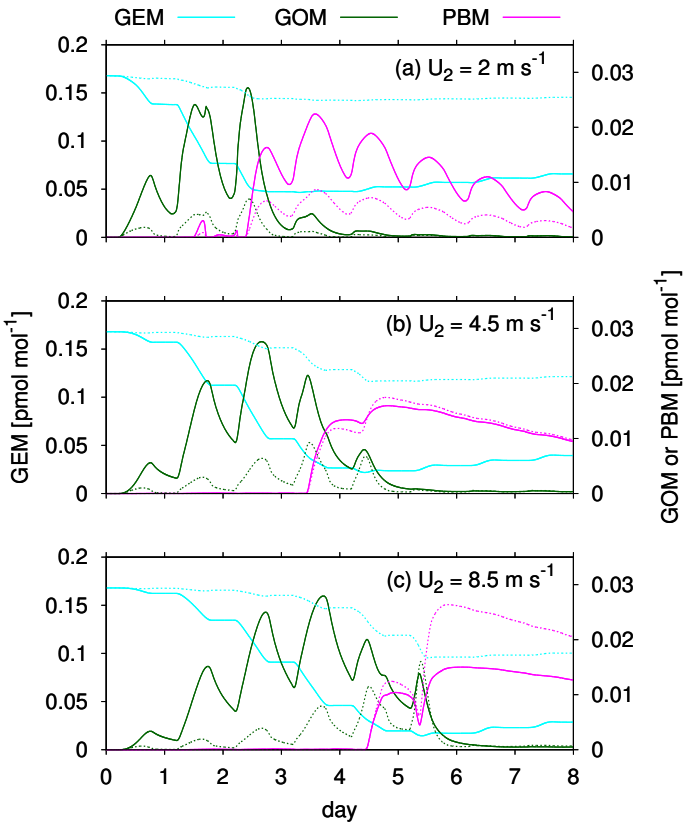

Fig. 7. Temporal evolution for the mixing ratios of GEM (light blue), GOM (dark green) and PBM (magenta) at the height of 1.5 m in the ambient air from model runs at U_2 = 2.0 m s^{-1} **(a)**, 4.5 m s^{-1} **(b)**, and 8.5 m s^{-1} **(c)**. Solid and dotted lines represent model runs with the gas-phase reaction HgBr + BrO switched on and off, respectively.

ACPD
13, 22151–22220, 2013

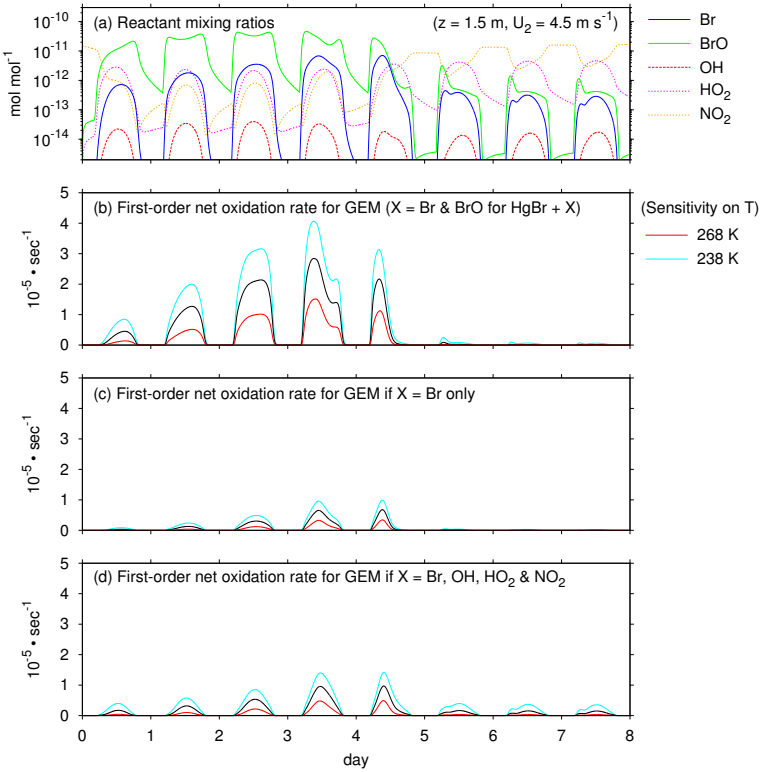

Fig. 8. **(a)** Temporal evolution for the mixing ratios of potential reactants (Br, BrO, OH, HO_2 and NO_2) for and HgBr in the gas phase at the height of 1.5 m in the ambient air from model runs at $U_2 = 4.5\,m\,s^{-1}$; **(b)** First-order net oxidation rates of GEM calculated at the same height from this model run (black line). Potential changes in the net GEM oxidation rates arising from changes in temperature are also estimated by raising (red line) and dropping (light-blue line) temperature by 15 K from 253 K for the calculation of rate constants for gas-phase Hg oxidation kinetics while all other physical and chemical parameters are calculated at 253 K; **(c)** The same as **(b)** but re-estimated by assuming only Br-atoms can react with HgBr to form a stable Hg(II) product (i.e., the reaction HgBr + BrO switched off); and **(d)** The same as **(c)** but re-estimated by assuming OH, HO_2 and NO_2 can react, in addition to Br, with HgBr to form stable Hg(II) products.

ACPD
13, 22151–22220, 2013

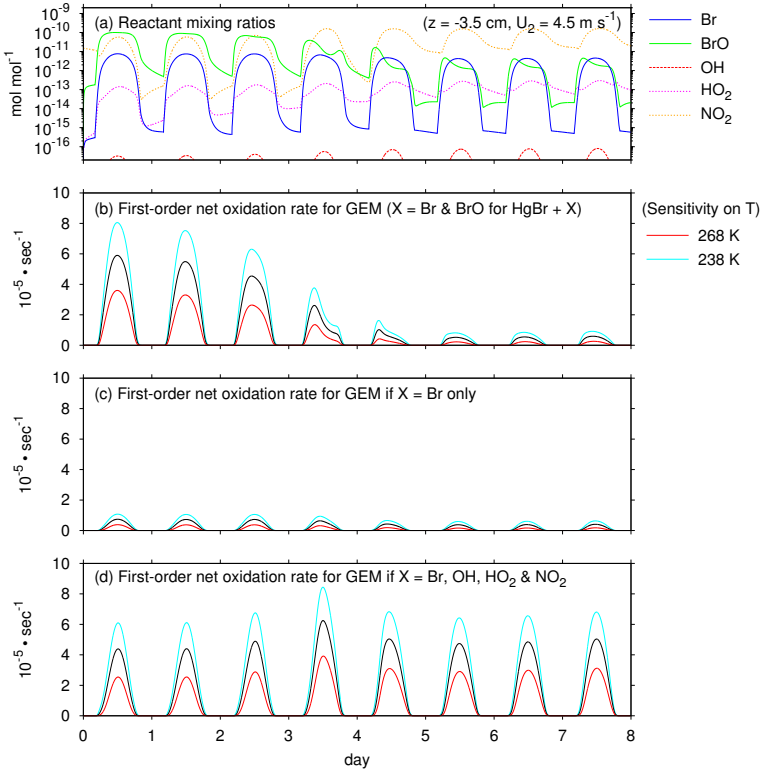

Fig. 9. The same as Fig. 8 but in the SIA at the depth of 3.5 cm.

ACPD
13, 22151–22220, 2013

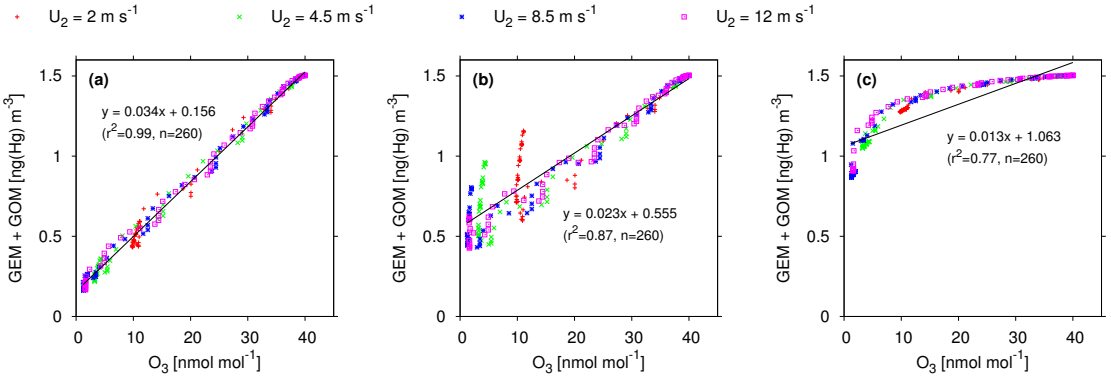

Fig. 10. Scatter plots of 3-hourly model output to show correlations between the concentrations of total gaseous mercury (GEM + GOM) and the mixing ratios of ozone at the height of 1.5 m in the ambient air as simulated in model runs at $U_2 = 2.0\,\mathrm{m\,s^{-1}}$, $4.5\,\mathrm{m\,s^{-1}}$, $8.5\,\mathrm{m\,s^{-1}}$, and $12.0\,\mathrm{m\,s^{-1}}$: **(a)** using a default chemical mechanism listed in Table 1 and the "slow" photo-reduction scenario based on Johnson et al. (2008) for in-snow Hg(II), **(b)** the same as **(a)** but using the "fast" photo-reduction scenario based on Kirk et al. (2006) for in-snow Hg(II), and **(c)** the same as **(a)** but with the gas-phase reaction HgBr + BrO being switched off. Units for the concentrations of total gaseous mercury and the mixing ratios of ozone are ng(Hg) per standard cubic meter (at 0 °C and 1 atm) and $\mathrm{nmol\,mol^{-1}}$, respectively, used for scatter plots of the same kind by Schroeder et al. (1998) and Ebinghaus et al. (2002).

ACPD
13, 22151–22220, 2013

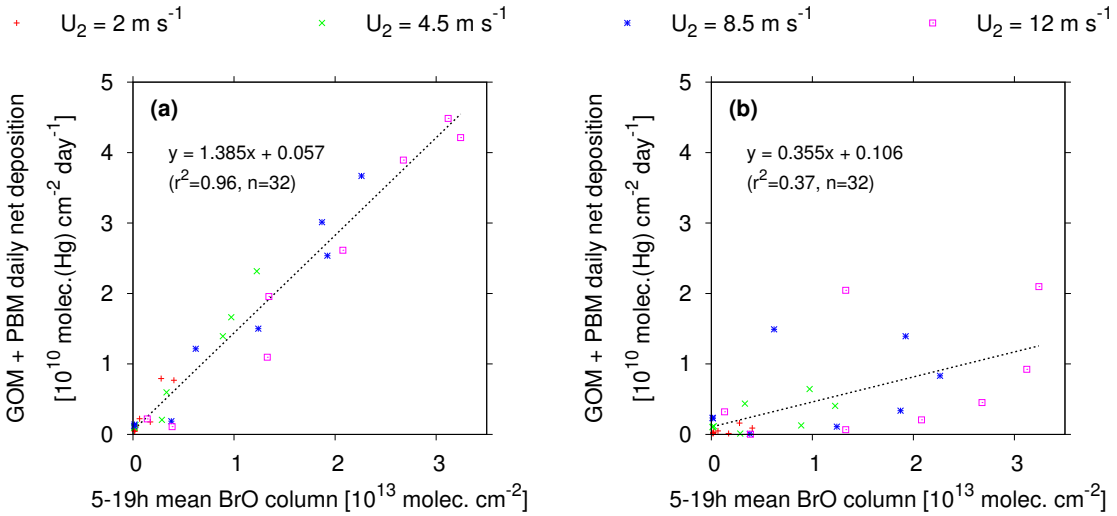

Fig. 11. Correlations between the daytime column amount of BrO in the atmosphere and the daily net deposition of GOM and PBM from the atmosphere to the snowpack on each simulated day (Day 1 to 8) in model runs at U_2 = 2.0 m s^{-1}, 4.5 m s^{-1}, 8.5 m s^{-1}, and 12.0 m s^{-1}: **(a)** using a default chemical mechanism listed in Table 1 and **(b)** the same as **(a)** but with the gas-phase reaction HgBr + BrO being switched off.

ACPD
13, 22151–22220, 2013

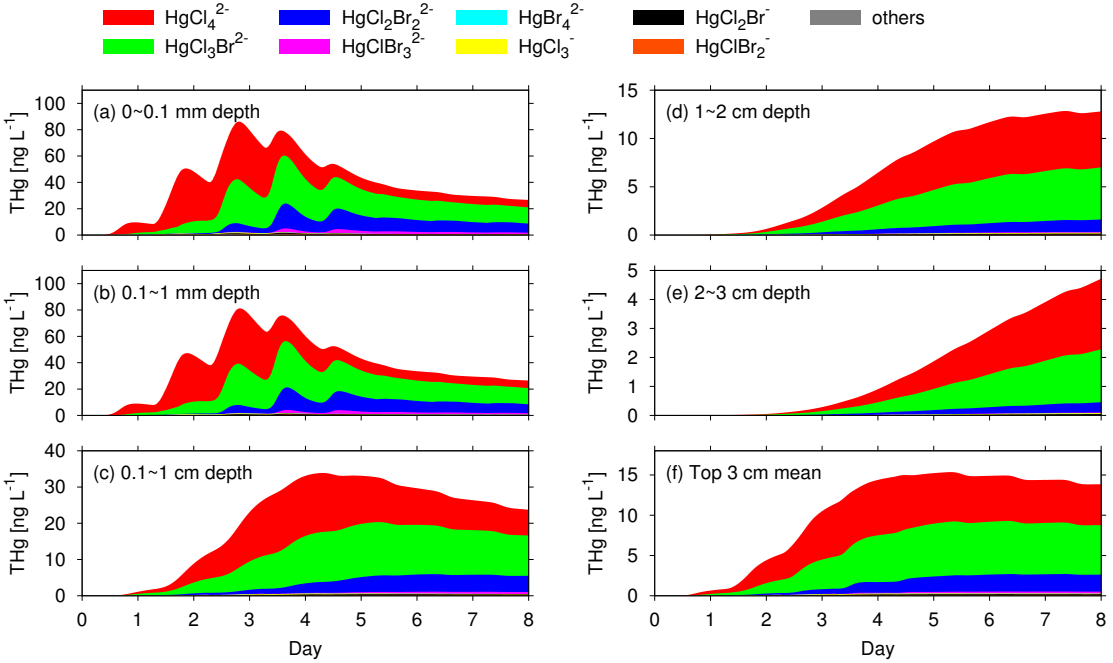

Fig. 12. Total concentrations and speciation of dissolved mercury in the top 3 cm of snowpack as simulated at $U_2 = 4.5\,\mathrm{m\,s^{-1}}$ using the "slow" in-snow Hg(II) photo-reduction scenario: **(a)** 0 ~ 0.1 mm depth (the topmost snowpack layer), **(b)** 0.1 ~ 1 mm depth, **(c)** 0.1 ~ 1 cm depth, **(d)** 1 ~ 2 cm depth, **(e)** 2 ~ 3 cm depth, and **(f)** average over the top 3 cm.

ACPD
13, 22151–22220, 2013

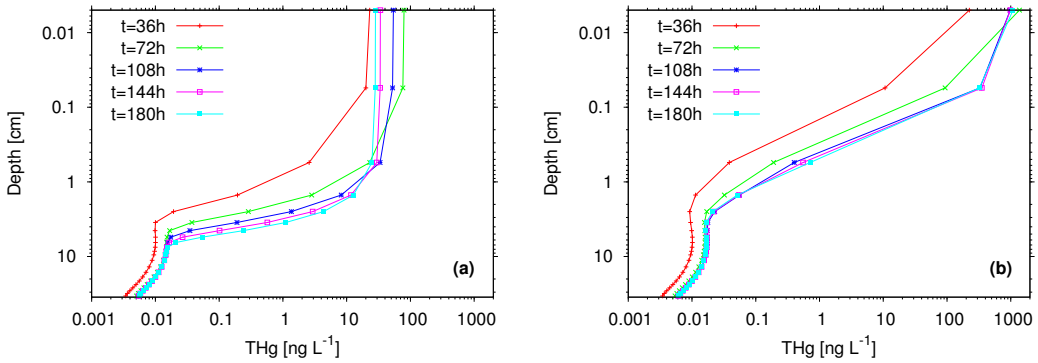

Fig. 13. Concentration profiles of total dissolved mercury as simulated in the model run at $U_2 = 4.5\,\mathrm{m\,s^{-1}}$ using the "slow" in-snow Hg(II) photo-reduction scenario: **(a)** the base case with vertical diffusion through the LLL network in the snowpack and **(b)** the case without vertical diffusion through the LLL network.

ACPD
13, 22151–22220, 2013

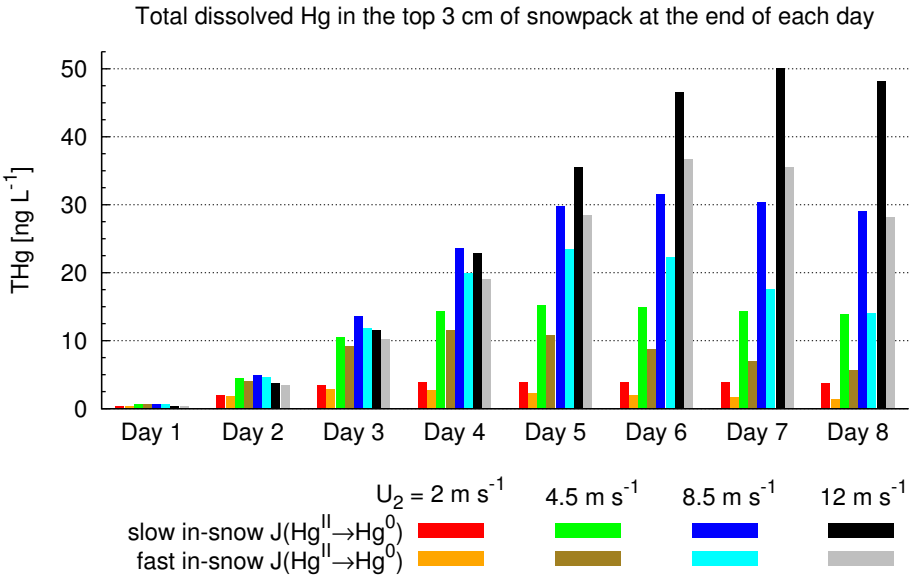

Fig. 14. Total concentrations of dissolved mercury averaged in the top 3 cm of snowpack at the end of each day (from Day 1 to Day 8) as simulated in model runs at U_2 = 2.0 m s^{-1}, 4.5 m s^{-1}, 8.5 m s^{-1}, and 12.0 m s^{-1} and for "slow" and "fast" in-snow Hg(II) photo-reduction scenarios.

ACPD
13, 22151–22220, 2013